Ordered Network Phases in Linear Poly(isoprene-*b*-styrene-*b*-ethylene oxide) Triblock Copolymers

Thomas H. Epps, III,† Eric W. Cochran,† Travis S. Bailey, Ryan S. Waletzko, Cordell M. Hardy, and Frank S. Bates*

Department of Chemical Engineering and Materials Science, University of Minnesota, Minneapolis, Minnesota 55455

Received June 22, 2004; Revised Manuscript Received August 14, 2004

ABSTRACT: The equilibrium phase behavior of 43 linear poly(isoprene-*b*-styrene-*b*-ethylene oxide) (ISO) triblock copolymer melts, with molecular weights that place these materials near the order−disorder transition, is reported. Ordered phase morphologies were characterized using small-angle X-ray scattering, transmission electron microscopy, dynamic mechanical spectroscopy, and static birefringence measurements. Interpretation of these results was aided by a modeling technique that facilitates resolution of reciprocal and real-space experimental data, leading to definitive three-dimensional morphological structures. Three distinct multiply continuous network morphologies are identified across a range of compositions between $0.1 \leq f_O \leq 0.3$, situated between two-domain and three-domain lamellae, where f_O represents the volume fraction of O blocks. Two cubic network phases, Q^{230} (core−shell double gyroid, $Ia\bar{3}d$ space group symmetry) and Q^{214} (alternating gyroid, $I4_132$ space group symmetry), flank an orthorhombic network phase, denoted O^{70} ($Fddd$ space group symmetry), which is positioned around the isopleth composition $f_S \approx f_I$. These results provide a powerful strategy for designing network phases in linear ABC triblock copolymers when $\chi_{AB} \approx \chi_{BC} < \chi_{AC}$, where χ represents the Flory−Huggins interaction parameter.

I. Introduction

ABC triblock copolymers offer the potential to create nanoscale morphologies with interesting and useful chemical and physical properties. However, cataloging the expansive ABC parameter space, relative to AB diblocks, presents a daunting task for experimentalists and theoreticians alike. A nearly complete understanding of neat linear diblock copolymers was achieved by the mid-1990s.[1,2] Phase behavior was sorted into four equilibrium two-domain morphologies: lamellae, hexagonally packed cylinders, spheres arranged on a BCC (or close-packed) lattice, and the double gyroid. The gyroid network covers a small portion of the phase diagram and until recently[3] appeared to be absent at higher segregation strengths.[2,4] Diblock phase behavior is governed by two parameters: volume fraction f_A and the product $\chi_{AB}N$, where χ_{AB} is the segment−segment interaction parameter and N is the total number of segments. This limited set of variables made feasible the comprehensive mapping of diblock copolymer phase behavior, from both experimental and theoretical perspectives.

More complex molecular architectures, such as linear and branched ABC triblocks, offer access to a wider spectrum of microstructured phase topologies. More than two dozen morphologies have been reported in linear ABC systems, including three-domain lamellae, core−shell versions of spheres, cylinders, and double gyroid,[1,5−8] alternating cylinders, spheres, and gyroid,[1,6,9−12] perforated structures,[5,6,13,14] and various other intricate microdomain assemblies.[1,6,15−17] This greater complexity is correlated with an increased number of independent molecular variables: three segment−segment interaction parameters, χ_{AB}, χ_{AC}, and χ_{BC}; two independent compositions, f_A, f_B ($f_C = 1 - f_A - f_B$); along with the overall degree of polymerization, N. In addition, block sequencing (and thus the sequence of interaction parameters) plays a critical role in establishing equilibrium morphologies. Though the increased number of parameters makes the task of triblock characterization more difficult, the rich ABC phase space continues to inspire intellectual curiosity and motivate interest in practical applications.

Network morphologies are especially enticing research targets. Percolating interconnected domains present an exciting opportunity to design materials with specific transport, structural, optical, and other properties that impact products such as membranes and low-density nanoporous materials. Three triply periodic network structures, based on linear ABC triblock copolymers, have been disclosed in the literature. Shefelbine and co-workers identified the pentacontinuous core−shell double gyroid in a poly(isoprene-*b*-styrene-*b*-dimethylsiloxane) (ISD) compound.[18] This structural assignment relied on the synergistic use of experimental and theoretical techniques that linked reciprocal space scattering data to real-space electron microscopy images. Matsushita and co-workers reported a triply continuous ("three-color") alternating gyroid in the poly(isoprene-*b*-styrene-*b*-vinylpyridine) (ISV) system; initially this structure was classified as a triple-diamond phase.[11,19] Matsen later showed that within self-consistent mean-field theory (SCFT) the alternating gyroid has a lower free energy than the triple diamond.[20] To the best of our knowledge, no diamond structure has been conclusively identified in any linear block copolymer. Bailey and co-workers [21] first proposed, and Epps et al. recently confirmed,[22] the triply periodic orthorhombic O^{70} network phase in a host of poly(isoprene-*b*-styrene-*b*-ethylene oxide) (ISO) triblock copolymers.

† These authors contributed equally to this work.

* To whom correspondence should be addressed: e-mail bates@cems.umn.edu.

10.1021/ma048762s CCC: $27.50
Published on Web 10/09/2004

Subsequently, Cochran and Bates discovered the O^{70} phase (and the companion (likely metastable) orthorhombic O^{52} phase) in poly(cyclohexylethylene-*b*-ethyl ethylene-*b*-ethylene) (CE_EE),[23] a fully saturated hydrocarbon system.

In a recent communication we showed that the orthorhombic O^{70} network phase occupies a sizable region near the center of the ISO phase portrait, bracketed by two cubic network phases, Q^{230} and Q^{214}, and two-domain (LAM_2) and three-domain (LAM_3) lamellar states.[22] This fascinating phase behavior was established through a combination of small-angle X-ray scattering (SAXS), transmission electron microscopy (TEM), light depolarization (birefringence), and dynamic mechanical spectroscopy (DMS) experiments, augmented by a morphology modeling effort.

This publication expands on our preliminary report, providing a comprehensive description of a systematic study of ISO phase space based on 43 triblock copolymers that span the region between two-domain IS lamellae and three-domain ISO lamellae. Triblock copolymers were produced from seven "parent" IS diblock copolymers, with $0.42 \leq f_S \leq 0.69$. Thus, all specimens lie on "isopleths" of constant f_S/f_I. Here we report the detailed characterization of these materials and substantiate our previous claims regarding the occurrence of the Q^{230} ($Ia\bar{3}d$, core−shell double gyroid), O^{70} ($Fddd$, orthorhombic network), and Q^{214} ($I4_132$, alternating gyroid) network phases. These networks are comprised of ordered arrays of trivalent, 10-node connected loops that form triply periodic lattices. We have achieved this level of understanding through a combination of experimental techniques, as mentioned above, meshed with mathematically generated level set models that bridge real and reciprocal space. These findings support a new strategy for designing block copolymer networks with linear ABC triblock copolymers.

II. Experimental Section

Synthesis and Chemical Characterization. Poly(isoprene-*b*-styrene-*b*-ethylene oxide) (ISO) triblock copolymers were prepared using a multistep anionic polymerization method, described in detail in a previous publication.[5] Only a brief synopsis is provided here. Aliquots of monohydroxy-terminated diblock copolymer, taken from a single parent batch of IS-OH, were initiated with potassium naphthenalide and reacted with specified amounts of ethylene oxide, leading to a set of homologous ISO triblock copolymers containing a common IS core and varying O block lengths. A total of 43 triblocks, belonging to seven isopleth families, were created in this way.

IS-OH diblock number-average molecular weights (M_n) and polydispersity indices (M_w/M_n) were determined using a combination of MALDI-TOF mass spectroscopy and high-performance size exclusion chromatography (SEC) (Phenomenex Phenogel columns coupled to a Wyatt Dawn DSP laser photometer using detectors at 18 angles and a Wyatt differential refractometer). Within expected error (roughly 5−10%) measured M_n values coincided with those anticipated by reaction stoichiometry. ISO molecular weights were deduced from the measured composition (see below) and the parent diblock values. SEC traces revealed no evidence of parent diblock copolymer, confirming efficient hydroxyl end-functionalization and subsequent reinitiation reactions.[24] Diblock and triblock polydispersity indices were calculated using SEC traces that were calibrated with poly(styrene) standards.

A Varian 300 NMR was used for composition analysis, with all samples dissolved in deuterated chloroform. Block mole fractions were determined using integrated ^{1}H NMR peak intensities and converted to volume fractions using published homopolymer densities reported at 140 °C ($\rho_I = 0.830$ g/cm^3, $\rho_S = 0.969$ g/cm^3, $\rho_O = 1.064$ g/cm^3).[25] The component volume fractions are listed in Table 1 for all samples investigated in this study. Density data were not corrected to reflect differences in temperature. Additional information regarding the characterizations procedures employed in this work can be found in Bailey et al.[5]

Synchrotron Small-Angle X-ray Scattering (SAXS). Synchrotron SAXS experiments were conducted on the DND-CAT at the Advanced Photon Source at Argonne National Laboratory using $\lambda = 0.827$ Å wavelength radiation. The sample-to-detector distance was 501 cm, and data were acquired on a Mar CCD area detector. Sample temperature was controlled in a liquid N_2-cooled DSC chamber under a helium purge. ISO specimens were heated above T_{ODT} (when possible) to erase effects due to thermal history and then cooled to 160 °C. Diffraction intensity was azimuthally averaged and is reported as a function of scattering wavevector modulus $q = |\mathbf{q}| = 4\pi/\lambda \sin(\theta/2)$, where θ is the scattering angle.

IT Characterization Facility (IT) SAXS. One- and two-dimensional SAXS patterns were collected at the University of Minnesota Institute of Technology Characterization Facility. The 1.54 Å Cu Kα X-rays were generated using a Rigaku RU-200BVH rotating anode equipped with a 0.2 × 2 mm microfocus cathode and total reflecting Franks mirror optics. 2D-SAXS data were collected with a Siemens HI-STAR multiwire area detector. The sample-to-detector distance was 230 cm. All SAXS data were corrected for detector response characteristics and plotted versus q. Sample temperature was controlled to within 0.5 °C during these measurements.

Transmission Electron Microscopy (TEM). TEM micrographs were collected on a JEOL 1210 TEM operating at 120 kV, located in the IT Characterization Facility. Samples (50−100 nm thickness) were prepared on a Reichart ultramicrotome using a Microstar diamond knife at −60 to −90 °C and placed on 400 mesh copper grids (Ted Pella). Electron scattering contrast was achieved by preferentially staining the I domains through exposure of cut specimens to the vapors of a 4% aqueous solution of OsO_4 (Ted Pella) for 5 min. Polymer samples were annealed prior to microtoming in the sample chamber of the IT-SAXS instrument and monitored by SAXS at various stages during the sample preparation process.

Static Birefringence. Light depolarization measurements were performed on 1 mm thick samples sealed in an argon atmosphere between two glass disks separated by an aluminum spacer. Each sample was placed in a heating chamber between crossed polarizers, and a 5 mW HeNe laser was directed through the polarizer sandwich. The specimen was heated or cooled at 1 °C/min using an electrically heated copper block and a PID controller to maintain heating/cooling rates. Transmitted depolarized intensity was detected using a photodiode connected to a voltmeter and normalized by the detector response with the polarizers in the parallel orientation, I_{max}. Birefringence is indicative of optical anisotropy.[26,27]

Dynamic Mechanical Spectroscopy (DMS). Mechanical spectroscopy experiments were conducted on a Rheometrics Scientific ARES strain-controlled rheometer using a parallel plate configuration with 25 mm diameter plates. Samples were typically 1 mm thick. Isochronal ($\omega = 1$ rad/s) dynamic elastic (G') and loss (G'') moduli measurements were collected during heating or cooling at 1 °C/min. For all measurements the strain amplitude was 1%, well within the linear viscoelastic regime. All isochronal and isothermal data acquisition was preceded by heating to disorder or 250 °C, whichever was lower, to erase thermal history. A more detailed description of DMS procedures can be found elsewhere.[21]

Differential Scanning Calorimetry (DSC). Calorimetry experiments were conducted on a Perkin-Elmer Pyris 1 differential scanning calorimeter with a Cryofill liquid nitrogen attachment. Melting points were associated with well-defined peaks in the heat input, measured during isobaric temperature ramps at constant heating rate (between 10 and 20 °C/min). The degree of crystallinity of the PEO domains was determined by the integration of the baseline-corrected melting peaks and referencing to the heat of fusion of bulk PEO (213 J/g).[28]

Table 1. ISO Characterization Data

polymer	M_n, Da	M_w/M_n	f_I[a]	f_S[a]	f_O[a]	phase	T_{OOT}, °C	T_{ODT}, °C	lattice dimensions, nm[b,c]
IS-2	12 700	1.04	0.58	0.42	0.00	DIS			
ISO-2e	15 200	1.06	0.50	0.36	0.14	Q^{230}		>200	42.8
ISO-2a	15 400	1.07	0.49	0.36	0.15	Q^{230}		>200	44.4
ISO-2b	16 300	1.07	0.46	0.34	0.20	Q^{230}		>250	47.0
ISO-2f	21 000	1.08	0.38	0.27	0.35	LAM_3		>250	24.0
IS-5	14 100	1.03	0.56	0.44	0.00	LAM_2		90	14.5 (80)
ISO-5b	16 100	1.06	0.50	0.39	0.11	Q^{230}		180	40.4
ISO-5c	17 700	1.06	0.46	0.36	0.18	Q^{230}		>200	45.5
ISO-5a	18 400	1.06	0.45	0.35	0.20	Q^{230}		>200	47.0
IS-9	13 700	1.05	0.53	0.47	0.00	LAM_2		85	14.7 (70)
ISO-9a	16 500	1.06	0.45	0.40	0.15	O^{70}		194	0.294, 0.582, 65.6
ISO-9b	18 200	1.06	0.41	0.37	0.22	O^{70}		>250	0.294, 0.582, 71.8
IS-3[d]	13 600	1.05	0.50	0.50	0.00	LAM_2		97	15.8 (85)
ISO-3a	13 800	1.05	0.49	0.49	0.02	LAM_2		111	16.1 (105)
ISO-3b	14 300	1.05	0.47	0.48	0.05	LAM_2		134	16.4 (100)
ISO-3c	14 600	1.06	0.47	0.47	0.07	LAM_2		146	16.9 (110)
ISO-3d	15 200	1.05	0.45	0.45	0.10	LAM_2		164	17.5 (110)
ISO-3e	15 800	1.05	0.44	0.44	0.13	O^{70}		194	0.294, 0.582, 65.4
ISO-3f	16 300	1.05	0.42	0.43	0.15	O^{70}		217	0.294, 0.576, 68.9
ISO-3g	16 900	1.06	0.41	0.41	0.18	O^{70}		246	0.294, 0.579, 70.5
ISO-3h	17 100	1.05	0.41	0.41	0.18	O^{70}		251	0.297, 0.585, 71.7
ISO-3i	17 800	1.06	0.39	0.40	0.21	O^{70}		267	0.292, 0.571, 74.6
ISO-3j	18 500	1.05	0.38	0.38	0.24	O^{70}		292	0.291, 0.582, 78.7
ISO-3k	19 400	1.06	0.36	0.37	0.27	LAM_3		>300	23.0
ISO-3l	20 400	1.05	0.35	0.35	0.30	LAM_3		>300	24.1
ISO-3m	21 800	1.06	0.33	0.33	0.34	LAM_3		>300	25.3
IS-16	12 500	1.05	0.44	0.56	0.00	DIS			
ISO-16a	13 200	1.06	0.42	0.53	0.05	LAM_2		90	15.8 (80)
ISO-16b	14 300	1.06	0.39	0.50	0.11	LAM_2		120	16.6 (110)
ISO-16d	16 500	1.06	0.35	0.44	0.21	O^{70}		>250	0.297, 0.578, 66.6
IS-1	16 100	1.04	0.39	0.61	0.00	DIS			
ISO-1e	18 700	1.06	0.31	0.55	0.14	Q^{214}		155	23.3 (150)
ISO-1a	19 400	1.07	0.32	0.51	0.17	Q^{214}		166	24.1 (150)
ISO-1f	19 700	1.06	0.32	0.52	0.16	$Q^{214} \rightarrow O^{70}$	130	180	24.1 (120)
ISO-1b	20 400	1.07	0.32	0.50	0.18	$Q^{214} \rightarrow O^{70}$	140	220	0.297, 0.580, 70.8
ISO-1c	22 200	1.07	0.30	0.46	0.24	O^{70}		>250	0.297, 0.580, 78.3
ISO-1k	22 300	1.08	0.30	0.45	0.25	O^{70}		>250	0.297, 0.580, 78.4
ISO-1h	24 700	1.08	0.27	0.42	0.31	LAM_3		>250	22.7 (175)
IS-15	12 500	1.02	0.31	0.69	0.00	DIS			
ISO-15a	14 500	1.05	0.27	0.56	0.17	Q^{214}		124	22.2 (110)
ISO-15b	16 700	1.04	0.25	0.53	0.22	$Q^{214} \rightarrow O^{70}$	140	166	0.297, 0.580, 65.0
ISO-15e	18 400	1.06	0.22	0.49	0.29	$Q^{214} \rightarrow O^{70}$	154	224	0.297, 0.580, 71.8
ISO-15f	18 900	1.07	0.21	0.48	0.31	LAM_3		>250	19.7

[a] Volume fractions are calculated from density data at 140 °C ($\rho_I = 0.83$ g/cm^3, $\rho_S = 0.969$ g/cm^3, $\rho_O = 1.064$ g/cm^3).[25] [b] Temperature is 160 °C unless otherwise noted in parentheses (°C). [c] Lattice dimensions listed for O^{70} samples correspond to *a*/*c*, *b*/*c*, and *c*. [d] These polymers correspond to ISOH-3 and ISO1 through ISO13, as originally published by Bailey et al. in ref 21.

Samples were stored in sealed containers at 0 °C for at least 2 weeks prior to use. Immediately before use, the sealed samples were allowed to thermally equilibrate at room temperature before a measured amount (between 3.5 and 6.5 mg) was sealed in a aluminum pan (#0219-0041, Perkin-Elmer). The system was cooled to −60 °C and allowed to thermally equilibrate prior to performing temperature scans. A heating scan was run up to 200 °C, followed by a cooling scan to −60 °C. First and second heating and cooling cycles were applied to all samples. Runs were repeated after samples had been stored at 0 °C for at least 2 more weeks to ensure reproducibility.

III. Results and Analysis

Figure 1, reproduced from our preliminary publication,[22] summarizes conclusions drawn from the full complement of characterization experiments described in this paper. ISO polymers (listed in Table 1) are located in the region of phase space bounded by $0.21 \leq f_I \leq 0.58$, $0.27 \leq f_S \leq 0.69$, and $0 \leq f_O \leq 0.35$. Ordered state morphologies and lattice dimensions, and order−order and order−disorder transition temperatures (T_{OOT} and T_{ODT}), also listed in Table 1, have been assigned on the basis of the integrated analysis of SAXS, DMS, TEM, and static birefringence measurements, as described in the following paragraphs.

We have identified five different phases in the ISO system: two-domain lamellae (LAM_2), three-domain lamellae (LAM_3), and three triply periodic network structures. Two cubic network phases, Q^{230} and Q^{214}, also known as double and alternating gyroids, and an orthorhombic network phase, O^{70}, are located at O block compositions intermediate to the LAM_2 and LAM_3 regions. O^{70} occupies a large central portion of the channel of network morphologies, flanked by Q^{230} (I-rich) and Q^{214} (S-rich). Figure 1 is a projection of phase behavior occurring over $100 < T < 250$ °C. We have identified Q^{214} at lower temperatures and O^{70} at higher temperatures in several specimens, separated by order−order phase transitions, as demarked by the overlapping portions of the red and violet regions in Figure 1. In the following sections, we present a detailed description of the procedures that resulted in these phase assignments.

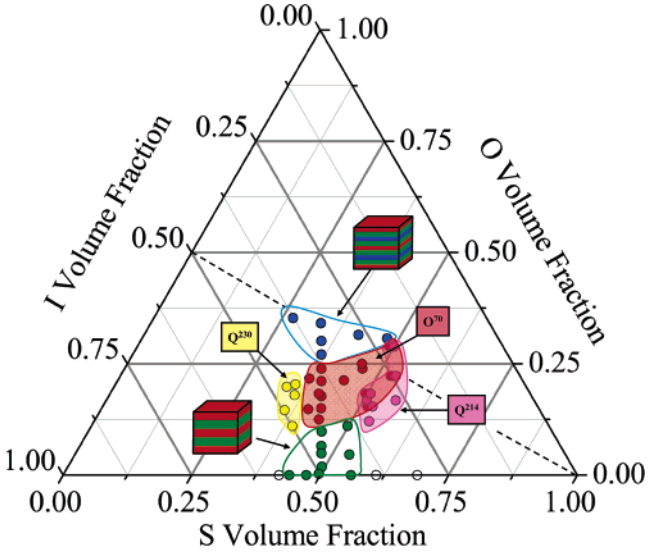

Figure 1. Poly(isoprene-*b*-styrene-*b*-ethylene oxide) (ISO) volume fraction phase portrait in the vicinity of the order−disorder transition. Filled and open circles indicate ordered and disordered states, respectively, within the experimental temperature range $100 \le T \le 225$ °C. Outlined areas identify compositions with two- and three-domain lamellae (identified by sketches), and shaded regions highlight the three network phases, Q^{230}, O^{70}, and Q^{214}. Overlap of the O^{70} and Q^{214} phase boundaries indicates the high- and low-temperature occurrence, respectively, of each phase. The dashed line identifies the condition $f_I = f_O$, associated with symmetric ISO molecules (adapted from ref 22).

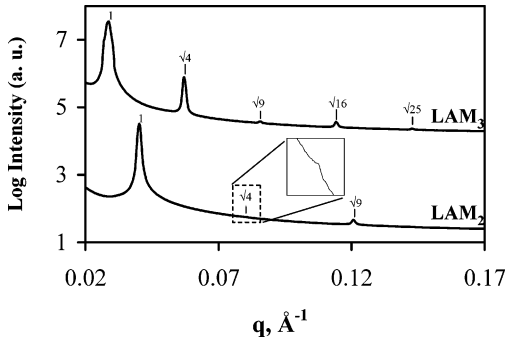

Figure 2. Synchrotron SAXS data for ISO-3l, a LAM_3 material (upper curve), and ISO-3c, a LAM_2 polymer (lower curve). Samples were prepared by cooling from above T_{ODT} followed by annealing and measurement at 130 °C. The diffraction peaks are indexed according to normalized peak moduli, where the primary peak is denoted q^*. The integral moduli values are indicative of lamellar morphologies for both curves. The $q^*\sqrt{4}$ peak in the LAM_2 specimen is nearly undetectable due to a structure factor extinction; the inset shows this peak at 10× vertical amplification. The upper curve is shifted vertically for clarity.

LAM_2 and LAM_3 Phases. Lamellae (LAM) phase assignments have been made on the basis of SAXS and TEM data. Figure 2 depicts SAXS patterns obtained from two specimens, ISO-3c (low O content) and ISO-3l (high O content), located on the symmetric ISO-3 isopleth. ISO-3c produced Bragg peaks located at q^*, $2q^*$, and $3q^*$ (the $2q^*$ peak is enlarged in the inset), where q^* is the primary peak position. The near absence of $2q^*$ scattering is consistent with a structure factor extinction for symmetric two-domain lamellae (LAM_2). Diffraction peaks from ISO-3l also appear at integral multiples with respect to q^*, with clear diffraction up to fifth order. Here the low intensity of the third-order diffraction peak is consistent with the structure factor extinction for symmetric three-domain lamellae (LAM_3). Calculations in support of these claims appear in the Appendix. The domain spacings, $d = 2\pi/q^*$, for all LAM_2 and LAM_3 assignments are listed in Table 1.

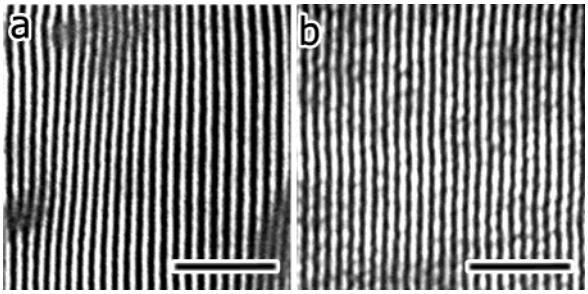

Figure 3. (a) TEM micrograph generated from ISO-3c, representative of the two-domain lamellar region (LAM_2) in Figure 1. (b) TEM micrograph generated from ISO-3l, representative of the three-domain lamellar region (LAM_3) in Figure 1. Dark regions in TEM micrographs result from OsO_4 staining of the poly(isoprene) domains. The unstained S and O domains appear much lighter (this statement applies to all micrographs in this work). Scale bars represent 100 and 166 nm for the LAM_2 and LAM_3 micrographs, respectively.

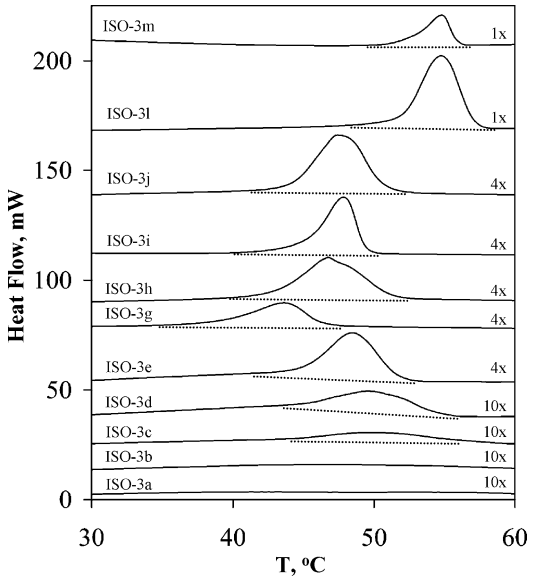

Figure 4. DSC endotherms near the PEO melting temperature for a number of ISO specimens along the $f_I = f_S$ isopleth (ISO-3 series). Curves have been baseline-subtracted and shifted vertically for clarity. Labels of 10×, 4×, or 1× indicate the factor of vertical magnification that has been employed to assist the visualization of the PEO melting transitions, which are denoted with dashed lines.

TEM micrographs from ISO-3c and ISO-3l, presented in Figure 3, support these lamellae assignments. Dark stripes correspond to OsO_4-stained I domains, while the light stripes account for unstained S and/or O domains. The SAXS and TEM experiments produced similar length scales; the results found in Figures 2 and 3 lead to $d_{SAXS} \approx d_{TEM}$ for ISO-3c and $d_{SAXS} \approx 1.17 d_{TEM}$ for ISO-3l. The minor discrepancy in the latter case may be due to O block crystallization, which likely produces the layer undulations evident in Figure 3b.

DSC experiments provided an estimate of O block crystallinity in each ISO specimen. A series of calorimetric traces, obtained while heating specimens drawn from the ISO-3 isopleth, from −60 to 100 °C, are shown in Figure 4. Specimens identified as LAM_3 exhibit a melting peak at about 54 °C, while those associated with

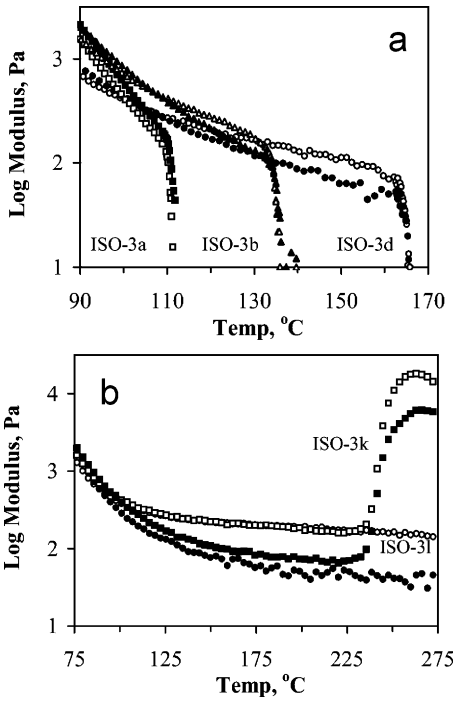

Figure 5. Isochronal G' (open symbols) and G'' (closed symbols) data from various lamellar ISO-3 series polymers. (a) ISO-3a (□, ■), ISO-3b (△, ▲), and ISO-3d (○, ●) specimens from the LAM_2 region. These samples feature nearly identical moduli that precipitously drop, indicating the lamellar-to-disorder transition, at successively higher temperatures. (b) ISO-3k and ISO-3l from the LAM_3 region. The sudden upturn in the moduli of ISO-3k at 238 °C is indicative of an order−order transition, but this phenomenon was not investigated further with X-ray scattering due to the high temperatures. ISO-3l remains ordered to temperatures beyond 300 °C.

the LAM_2 state display a significantly smaller endotherm that peaks at 48−50 °C; at intermediate compositions (O^{70} phase, see below) O block melting occurs at 43−48 °C. Integration of these endothermic peaks, followed by normalization by the weight percent O block and the heat of fusion for poly(ethylene oxide) crystals (213 J/g),[28] yielded the O block percent crystallinity. For all ordered ISO specimens identified in Figure 1, except those labeled LAM_2, this value was between 50% and 60%.[21] In contrast, those identified as LAM_2 were determined to have at most 20% crystallinity, consistent with significant mixing between O and S blocks. These results support our two-domain LAM_2 assignments and the LAM_3 and other three-domain microstructures, consistent with our earlier report.[21]

Isochronal DMS measurements, obtained while heating specimens at 1 °C/min, were used to establish the location of LAM-to-disorder phase transitions in these materials. Figure 5a illustrates the linear viscoelastic response of ISO-3a, ISO-3b, and ISO-3d. At well-defined temperatures the dynamic elastic (G') and loss (G'') moduli drop discontinuously, signaling the order−disorder transition (ODT); increasing the O block length leads to a higher T_{ODT}. Within the ISO-3 series the LAM_3 structures (Figure 5b) remain ordered up to the highest measurement temperature (275 °C). A sharp increase in G' and G'' occurs at 238 °C with specimen ISO-3k, suggestive of an order−order transition (OOT). This high-temperature state was not characterized by SAXS for fear of degrading the specimen. However, proximity to the O^{70} phase region (specimen ISO-3j, see

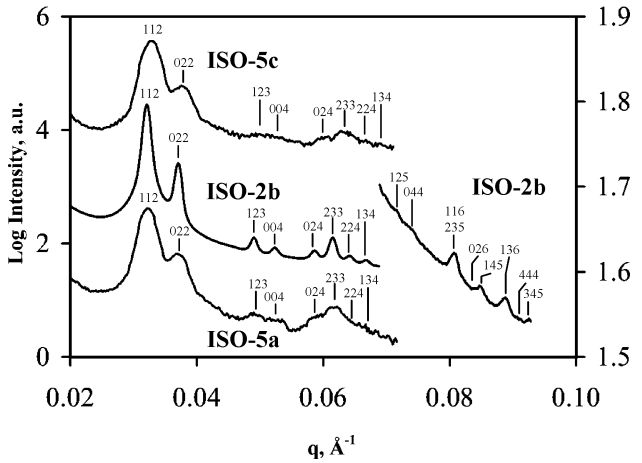

Figure 6. Azimuthally integrated SAXS data for ISO-5c (IT characterization), ISO-2b (APS synchrotron), and ISO-5a (IT characterization) are presented in the upper, middle, and lower curves, respectively. Samples were prepared by annealing at 200 °C followed by annealing and measurement at 160 °C. The data are characteristic of the Q^{230} ($Ia\bar{3}d$) morphology. The higher-order synchrotron data (middle curve) are plotted with respect to the secondary y-axis. The curves are shifted vertically for clarity.

Table 1 and text below) suggests a LAM_3 to O^{70} transition.

Q^{230} (Core−Shell Double Gyroid) Phase. Six triblock copolymers, belonging to the ISO-2 and ISO-5 series (see Table 1) and labeled with yellow symbols in Figure 1, produced a complement of characterization results consistent with a Q^{230} phase assignment. Here we highlight these findings.

SAXS powder patterns taken at the Advanced Photon Source (APS) and the University of Minnesota IT Characterization facility provided the basis for making an ordered state space group assignment. Figure 6 shows representative scattering from ISO-2b, ISO-5a, and ISO-5c. We acquired the pattern for ISO-2b at the APS, which provides an excellent signal-to-noise ratio and the best q resolution, enabling the identification of numerous Bragg reflections with relative peak positions at $q/q^* = \sqrt{6}$, $\sqrt{8}$, $\sqrt{14}$, $\sqrt{16}$, $\sqrt{20}$, $\sqrt{22}$, $\sqrt{24}$, $\sqrt{26}$, $\sqrt{30}$, $\sqrt{32}$, $\sqrt{34}$, $\sqrt{38}$, $\sqrt{40}$, $\sqrt{42}$, $\sqrt{46}$, $\sqrt{48}$, and $\sqrt{50}$. (The principal peak corresponds to $q^*\sqrt{6}$ and $q^* = q_{001}$ as discussed below.) This sequence is uniquely consistent with the cubic $Ia\bar{3}d$ space group,[18,29,30] and Miller indices are assigned in Figure 6 according to Bragg's law. The ISO-5a and ISO-5c patterns, collected at the IT Characterization Facility, contain fewer identifiable reflections due to a lower instrument resolution and beam intensity. Nevertheless, the overall SAXS patterns are consistent with the synchrotron result, particularly the location and relative intensities of the first and second reflections. The lattice dimensions for the Q^{230} materials ($d_{001} = 2\pi/q^*$) appear in Table 1.

TEM micrographs were generated for all samples in this region. Figure 7a displays a micrograph with p6 plane group symmetry, a "wagon-wheel" pattern with 3-fold junctions forming the "spokes" of the wheels. This image has been described in reports detailing the core−shell double gyroid.[5,18] The projection in Figure 7b further demonstrates domain connectivity, and 3-fold connections appear to be the basic constructor.

Birefringence measurements were employed to assess the optical properties of materials in this region. Optically isotropic morphologies, such as cubic structures

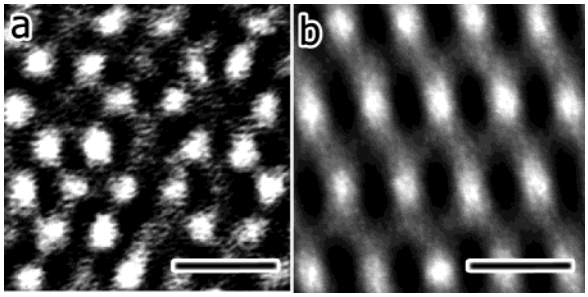

Figure 7. (a) TEM micrograph of ISO-2a showing a projection with p6 plane group symmetry. This image resembles the "wagon-wheel" pattern, similar to projections from double-gyroid materials reported by Bailey et al.[5] and Shefelbine et al.[18] (b) TEM micrograph from the same material displaying another direction that shows domain continuity. Scale bars in each panel represent 30 nm. Simulated TEM micrographs used for direction assignment appear in Figure 23.

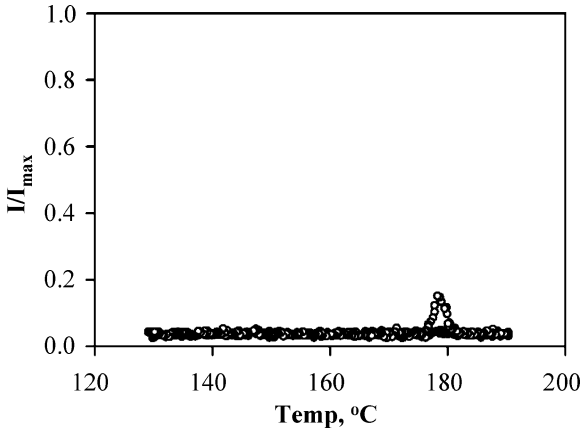

Figure 8. Birefringence data for ISO-5b, located in the Q^{230} region in Figure 1, during heating (●) and cooling (○). The lack of significant transmitted light intensities either above or below T_{ODT} is consistent with cubic ($T < T_{ODT}$) and disordered ($T > T_{ODT}$) assignments. The small signal in the cooling data at T_{ODT} is repeatable and is likely a result of grain reorganization or a transient intermediate phase.[31−33]

and the disordered state, lack a unique optical axis and are thus nonbirefringent. Figure 8 shows normalized light depolarization data recorded during heating and cooling for ISO-5b. On heating, only baseline intensity values are found for both the ordered and disordered states. During cooling, a small transient signal appears, beginning at 181 °C (corresponding to T_{ODT}) and then collapsing at about 175 °C. This reproducible phenomenon signals an optically active transient state, which forms as the disordered melt assembles into the equilibrium gyroid morphology.[31−33] The absence of birefringence in ordered ISO-5b is consistent with a cubic assignment.

Isothermal frequency DMS experiments were conducted to investigate the linear viscoelastic properties of the region denoted Q^{230}. Figure 9 presents representative data sets obtained between 120 and 200 °C from ISO-2b, in unshifted (upper panel) and time−temperature superimposed (TTS) (lower panel) forms. A plateau in G' indicates solidlike behavior over a wide range of time scales, a distinctive feature of triply periodic structures.[34]

All Q^{230} materials show similar behavior and exhibit scattering, mechanical, and optical properties consistent with previously reported core−shell gyroid materials.[5,18,29] The peak locations and relative intensities

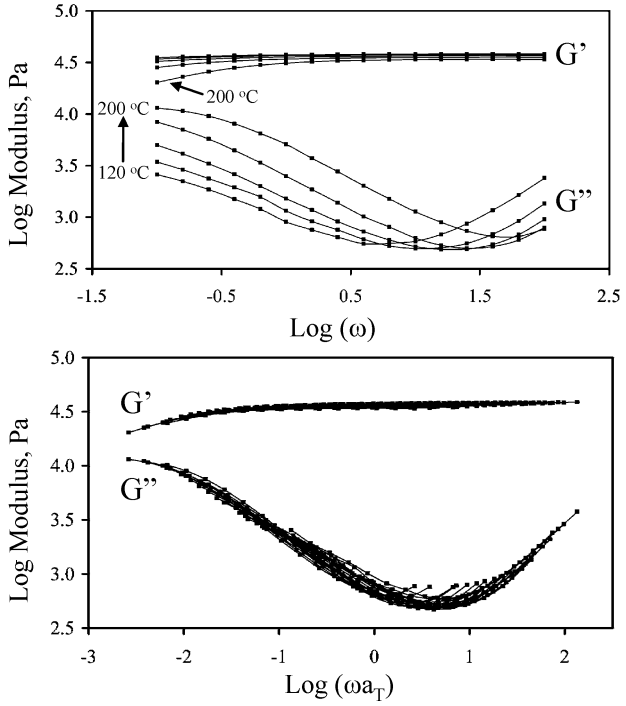

Figure 9. Isothermal frequency scans for ISO-2b in the Q^{230} region of Figure 1. log G' (upper curves) and log G'' (lower curves) appear in each panel. (a) Superimposition of scans from $\omega = 0.1$ to 100 rad s^{-1} at 20 °C increments from 120 to 200 °C. (b) Frequency sweep data acquired at 10 °C increments between 120 and 200 °C, shifted according to time−temperature superposition ($T_{ref} = 110$ °C). The large plateau in G' over a wide frequency range is distinctive of triply periodic order.

(SAXS), 3-fold symmetry and network connectivity (TEM), optical isotropy (lack of birefringence), and solidlike behavior characteristic of triply periodic structures (DMS) provide clear evidence that the region labeled Q^{230} in Figure 1 corresponds to the core−shell double gyroid network morphology.

O^{70} (Orthorhombic Network) Phase. The largest region of the phase portrait, denoted O^{70} (red circles, Figure 1), includes 15 specimens, drawn from the ISO-9, ISO-3, ISO-16, ISO-1, and ISO-15 polymer series (Table 1). The associated characterization results are presented in this section.

Synchrotron SAXS powder patterns for several samples (taken at 160 °C) are shown in Figure 10. Each diffraction pattern contains a rich assortment of peaks with slightly varying positions from specimen to specimen. The similarity of these patterns suggests a common space group symmetry. In each pattern, there is a broad, often visibly asymmetric first-order peak, followed by a series of lower intensity higher order reflections. For example, ISO-3h produced SAXS peaks located at q/q^* = 1, 1.50, 2.53, 3.06, 3.23, 3.72, 3.97, 4.15, 4.76, 5.26, 5.64, 6.04, 6.29, 7.09, 7.30, 8.39, 9.84. This complicated sequence does not conform to a cubic, tetragonal, or hexagonal Bravais lattice. However, an orthorhombic lattice, for which $q_{hkl} = 2\pi[h^2/a^2 + k^2/b^2 + l^2/c^2]^{1/2}$, accounts for these locations with the appropriate choice of lattice dimensions a, b, and c, where h, k, and l are the associated Miller indices. Table 1 enumerates the best least-squares values of a/c, b/c, and c for all O^{70} specimens at 160 °C (unless noted otherwise); values vary slightly from specimen to specimen. These choices of lattice dimensions lead to the indexing scheme that

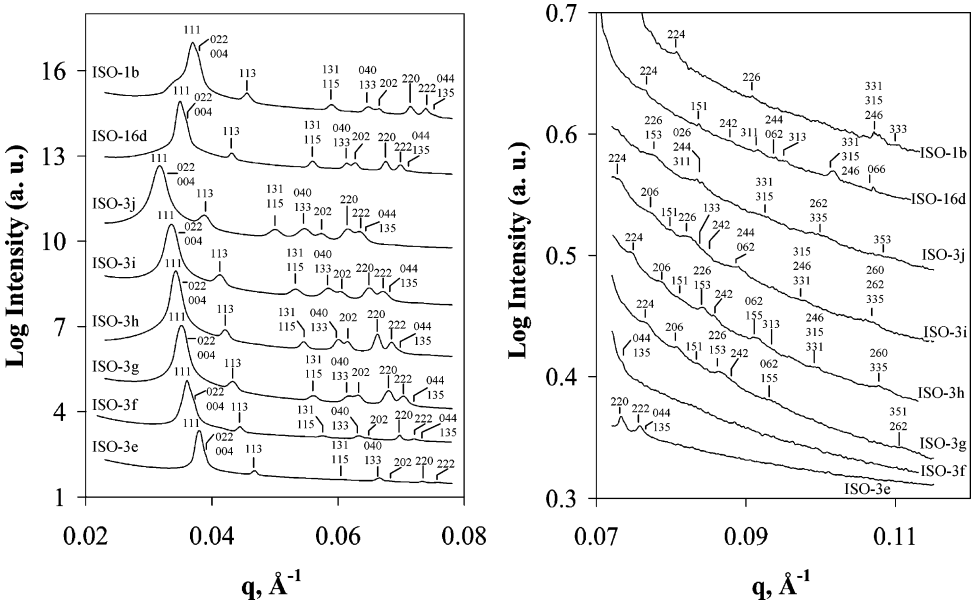

Figure 10. Azimuthally integrated synchrotron SAXS data for several specimens in the O^{70} region of Figure 1. Samples were prepared by annealing at 225 °C for 15 min followed by annealing and measurement at 160 °C. All scattering curves are indexed based on *Fddd* symmetry using the lattice constants listed in Table 1. Shifts in relative peak locations are a consequence of slight variations in relative lattice dimensions with composition. Higher-order data are displayed in the right panel. The curves are shifted vertically for clarity.

appears as peak labels in Figure 10. This lattice model consistently places the 111, 022, and 004 reflections within the range of the broad first-order peak, with the 022 and 004 positions in agreement with the position of the high-q shoulder. The 113, 131, 115, 040, 133, 202, 220, 222, 044, and 135 positions are also in agreement with measured peak locations. Absent reflections precisely match the extinction rules for *Fddd* (#70) space group symmetry; additionally, there are no *Fddd*-allowed peaks that cannot be identified in the low-order data (i.e., for $q_{hkl} \leq q_{135}$). High-order reflections (Figure 10, right panel) are also allowed by *Fddd* symmetry according to our selection of lattice dimensions. The locations of these high-q reflections are quite sensitive to small changes in lattice parameters. In most cases, the 224 and 226 reflections are visible; however, other reflections become more or less intense depending on interactions between the form and structure factors.

Extensive use of TEM provided a number of structural details about these polymers. Collections of micrographs from various samples in the region contained similar patterns, supporting the notion that each sample shares a common morphology. Micrographs for ISO-1c, appearing in Figure 11, are representative examples of the two most predominant views. In each micrograph, there is no discernible contrast between bright S and O domains, while OsO_4-stained I domains appear dark. The pattern in Figure 11a appears to contain pmg plane group symmetry, with staggered rows of bright elliptical spots interconnected with an array of trivalent connections. Figure 11b also is suggestive of pmg symmetry, featuring offset rows of bright, slightly ellipsoidal spots partitioned by dim connective stripes. Closer inspection of the bright spots reveals further structural details such as an "X" pattern, suggesting that these locations represent intersections of S/O-rich "stripes". The domain connectivity that may be inferred from these two distinct views suggests the morphology is a triply periodic continuously percolating network structure. Though Figure 11a is reminiscent of Figure 7b, and Figure 11b is superficially similar to Figure 16b (TEM from Q^{214} region, see next section), all micrographs from this region lack regions of true 3-fold and 4-fold symmetry. The absence of these symmetries, common to cubic structures, is consistent with an orthorhombic space group assignment.

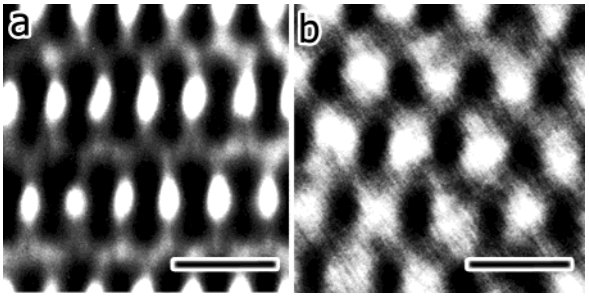

Figure 11. (a) TEM micrograph generated from ISO-1c, representative of a number of samples from the O^{70} region (see Figure 1). Bright ovals interconnected with trivalent junctions are characteristic of the network topology. (b) TEM micrograph from the same material depicting a complementary projection. Scale bars in each panel represent 30 nm. Simulated TEM micrographs confirming the experimental direction assignments appear in Figure 23.

ISO materials in the O^{70} region possess significant optical activity. Figure 12 presents birefringence data with normalized transmitted light intensity plotted vs temperature for ISO-9a. Heating and cooling scans were conducted at 1 °C/min. As the sample is cooled from 205 °C, a step increase in transmitted intensity occurs at 186 °C. The intensity increases steadily as the sample is cooled to 120 °C. The subsequent heating curve superimposes on the cooling data except for an 8 °C hysteresis region beginning at 186 °C, after which the transmitted intensity returns immediately to the baseline value. SAXS of this material (not shown) exhibits a diffraction pattern similar to those in Figure 10 below 186 °C, and correlation-hole scattering above 194 °C, allowing the step transitions in Figure 12 to be associated with the ODT. The hysteresis in the data indicates that this transition is reversible and weakly first order.

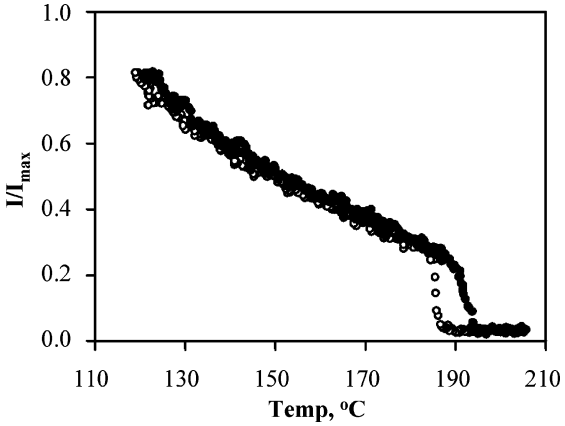

Figure 12. Birefringence data for ISO-9a located in the O^{70} region in Figure 1. Light depolarization intensity was determined on heating (●) and cooling (○). Depolarization of light (birefringence) is consistent with orthorhombic symmetry, while the absence of optical activity at higher temperatures supports the disordered state assignment. Hysteresis in the birefringence heating and cooling measurements is indicative of a weakly first-order phase transition.

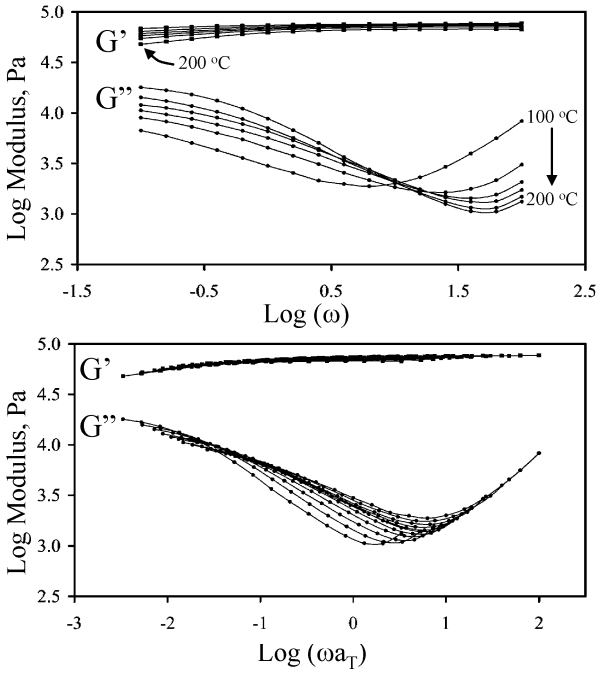

Figure 13. Isothermal frequency scans between 100 and 200 °C for ISO-3g in the O^{70} region of Figure 1. log G' (upper curves) and log G'' (lower curves) appear in each panel. (a) Superimposition of scans from $\omega = 0.1$ to 100 rad s^{-1} at 20 °C increments. (b) Frequency sweep data at 10 °C increments, shifted to a reference temperature $T_{ref} = 110$ °C according to time−temperature superposition. The large plateau in G' over a wide frequency range is distinctive of triply periodic order.

The large birefringence signal produced by ordered ISO-9a is a consequence of the optical anisotropy of the morphology; these data confirm that samples from the O^{70} region are noncubic, since cubic structures are optically isotropic over mesoscopic length scales.

Figure 13 displays representative DMS data for ISO-3g. In the upper panel, a series of isothermal frequency spectra feature a large elastic plateau modulus, characteristic of triply periodic morphologies. Time−temperature superposition produces a satisfactory, although not perfect, master curve. Isochronal heating and cooling (1 °C/min, not shown) revealed T_{ODT} at 246 °C.

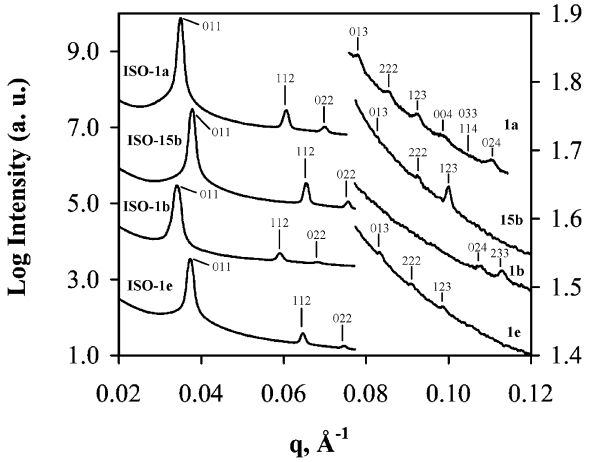

Figure 14. Azimuthally integrated APS SAXS data for ISO-1a, ISO-15b, ISO-1b, and ISO-1e (from top to bottom). Samples were prepared by cooling from above T_{ODT}, followed by annealing and measurement at 160 °C. Higher-order data are plotted using a secondary y-axis. All curves are uniquely indexed with $I4_132$ space group symmetry. Curves are shifted vertically for clarity.

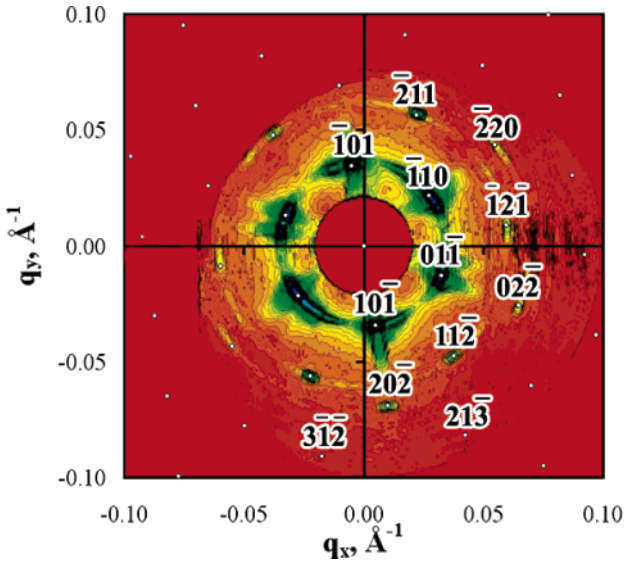

Figure 15. Representative 2D SAXS pattern for an annealed Q^{214} sample, ISO-1a, at 160 °C. Slow ordering of the network phase 5 °C below T_{ODT} (166 °C) results in the growth of large well-defined grains, scattering from which reveals portions of the reciprocal lattice that are readily indexed with the $I4_132$ assignment.

The SAXS, TEM, birefringence, and DMS data collectively indicate that ISO polymers in the composition region labeled O^{70} in Figure 1 form a noncubic, triply periodic network morphology with *Fddd* space group symmetry. In the Modeling section, we return to the SAXS and TEM data to infer the topology of this microstructure.

Q^{214} (Alternating Gyroid) Phase. The region denoted Q^{214} is located on the S-rich side of the complex phase channel (see Figure 1) and includes seven specimens drawn from the ISO-1 and ISO-15 series (see Table 1). Several of the samples in this region exhibit an OOT; this phase transition is discussed in the next section.

Synchrotron SAXS powder patterns for several samples identified with the Q^{214} phase are shown in Figure 14. Diffraction peaks are evident at positions $q/q^* = \sqrt{2}$,

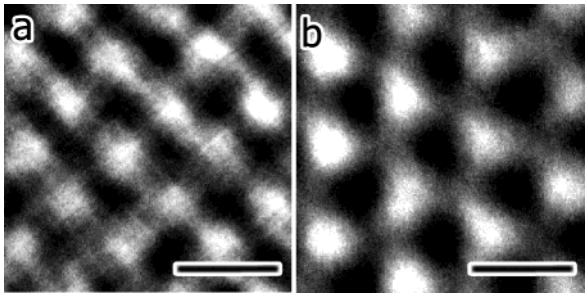

Figure 16. (a) TEM micrograph from ISO-1a, representative of samples from the Q^{214} region (see Figure 1). This direction shows a 4-fold axis of the network topology. (b) TEM micrograph generated from the same material showing a direction with a 3-fold axis. Scale bars in each panel represent 30 nm. Simulated TEM micrographs used for direction assignment appear in Figure 23.

$\sqrt{6}$, $\sqrt{8}$, $\sqrt{10}$, $\sqrt{12}$, $\sqrt{14}$, $\sqrt{16}$, $\sqrt{18}$, and $\sqrt{20}$. (The principal peak corresponds to $q^*\sqrt{2}$ and $q^* = q_{001}$; see below.) This sequence of reflections indicates cubic symmetry, and the absence of $q^*\sqrt{4}$ scattering excludes all but $I4_132$ (#214) space group symmetry. Miller indices appear in Figure 14 for each diffraction pattern, and lattice constants ($d_{001} = 2\pi/q^*$) are listed in Table 1 for all Q^{214} samples.

A 2D-SAXS diffraction pattern, obtained between 30 and 60 min after cooling specimen ISO-1a from 10 deg above, to 5 deg below, T_{ODT} is presented in Figure 15. This image contains a limited number of diffraction spots, rather than the conventional powder pattern. We interpret this distinctive SAXS pattern as resulting from nucleation limited ordering, which produces relatively few large grains, several of which satisfy the Bragg condition, revealing portions of the reciprocal lattice. As noted in Figure 15, the $01\bar{1}$, $10\bar{1}$, $11\bar{2}$, $02\bar{2}$, $20\bar{2}$, $21\bar{3}$, and $31\bar{2}$ reflections are well-defined, and the angular relationships support the $I4_132$ (Q^{214}) assignment obtained from powder pattern data.

TEM micrographs (Figure 16) provide direct visual evidence of the polymer microstructure. Figure 16a highlights a TEM projection with p4m plane group symmetry. The dark areas correspond to OsO_4-stained I domains. Figure 16b presents a different projection displaying 3-fold symmetry (p3m1). The prevalence of 3-fold and 4-fold symmetry in micrographs from specimens located in the region labeled Q^{214} in Figure 1 is consistent with a cubic microstructure.

Birefringence measurements were again used to assess optical activity. Figure 17 displays light depolarization data obtained while heating and cooling (1 °C/min) sample ISO-15a ($T_{ODT} = 124$ °C). A lack of optical activity (birefringence) is consistent with the cubic space group assignment. Curiously, this material does not show any evidence of the ODT.

DMS experiments probed the viscoelastic properties of these materials. Figure 18 shows representative isothermal frequency sweeps (upper panel) and a time−temperature superimposed master curve (lower panel). A prominent plateau in G' is indicative of a triply periodic structure.

SAXS diffraction and systematic absences unique to $I4_132$ in one- and two-dimensional scattering data, 3- and 4-fold projections revealing network connectivity (TEM), optically inactivity (lack of birefringence), and solidlike behavior over several decades of frequency (DMS) provide clear evidence that the region labeled

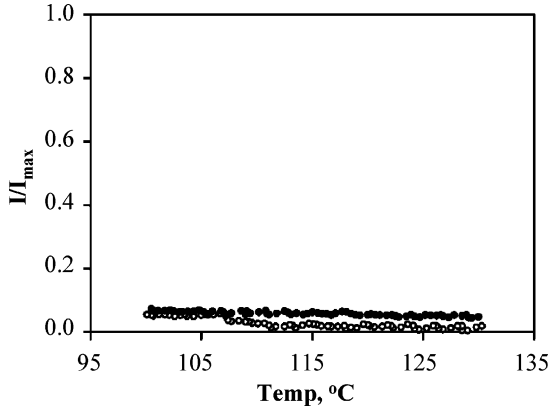

Figure 17. Birefringence data for ISO-15a, located in the Q^{214} region in Figure 1. Light depolarization intensities were determined during heating (●) and cooling (○). The lack of significant transmitted intensity either above or below T_{ODT} is consistent with cubic ($T < T_{ODT}$) and disordered ($T > T_{ODT}$) assignments.

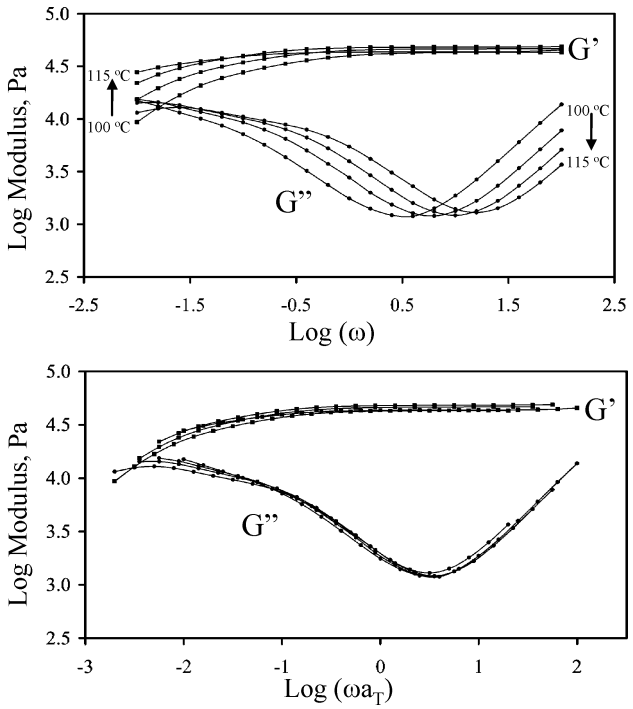

Figure 18. Isothermal DMS results for ISO-15a in the Q^{214} region of Figure 1, from 100 to 115 °C at 5 °C. log G' (upper curves) and log G'' (lower curves) appear in each panel. (a) Superimposition of scans from $\omega = 0.1$ to 100 rad s^{-1}. (b) The identical data, shifted according to time−temperature superposition ($T_{ref} = 110$ °C). The large plateau in G' over a wide frequency range is distinctive of triply periodic order.

Q^{214} in Figure 1 corresponds to the alternating gyroid network morphology.

Q^{214} to O^{70} Order−Order Transition (OOT). SAXS data (lab-based instrument), obtained from ISO-15b at 100, 150, and 200 °C, are presented in Figure 19. Three orders of diffraction are evident at the lowest temperature, with $q/q^* = \sqrt{2}$, $\sqrt{6}$, and $\sqrt{8}$. This pattern is consistent with those associated with the Q^{214} assignment (see Figure 14). A different scattering pattern develops when the material is heated to 150 °C, indicating a transformation to another microstructure. This SAXS "fingerprint" resembles the patterns identified as O^{70} (Figure 10) and has been indexed accordingly. At 200 °C, a single broad SAXS peak was recorded,

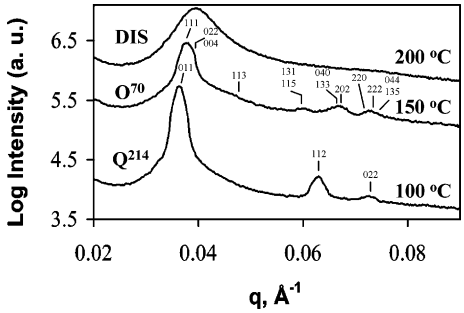

Figure 19. SAXS data at 100, 150, and 200 °C for ISO-15b of the O^{70}/Q^{214} overlap region in Figure 1. The sample was heated to 200 °C and annealed for 1 h at each temperature before data collection. Displayed data were acquired during a second heating run. The upper curve (200 °C) shows the disordered state, characterized by a broad low-intensity peak. The middle curve (150 °C) displays peaks characteristic of the O^{70} morphology and is indexed according to the orthorhombic *Fddd* space group. The lower curve (100 °C) is indexed according to the cubic $I4_132$ space group. The curves are shifted vertically for clarity.

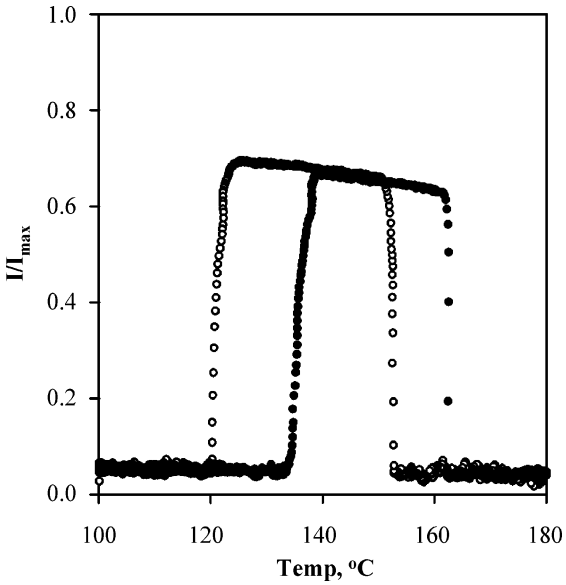

Figure 20. Birefringence data for ISO-15b from the O^{70}/Q^{214} overlap region in Figure 1. Light depolarization intensities were determined during heating (●) and cooling (○). Birefringence at intermediate temperatures is consistent with orthorhombic (O^{70}) symmetry, while the absence of optical activity at higher and lower temperatures supports assignments of disorder and cubic (Q^{214}) symmetry, respectively. Hysteresis between the heating and cooling birefringence measurements indicates a weakly first-order phase transition.

consistent with correlation-hole scattering from the disordered state; DMS measurements indicate T_{ODT} = 166 °C (see Table 1).

The optical properties of ISO-15b were probed between 100 and 180 °C, while heating and cooling the material at 1 °C/min. At low and high temperatures the polymer is not birefringent, as illustrated in Figure 20. However, at intermediate temperatures (between 137 and 162 °C on heating and 152 and 120 °C on cooling) significant rotation of light was recorded. These results indicate the presence of two optically isotropic, and one anisotropic, states separated by two first-order (i.e., hysteretic) transitions. On the basis of the SAXS results presented in Figure 19, we associate these three optical responses with the Q^{214}, O^{70}, and disordered phases.

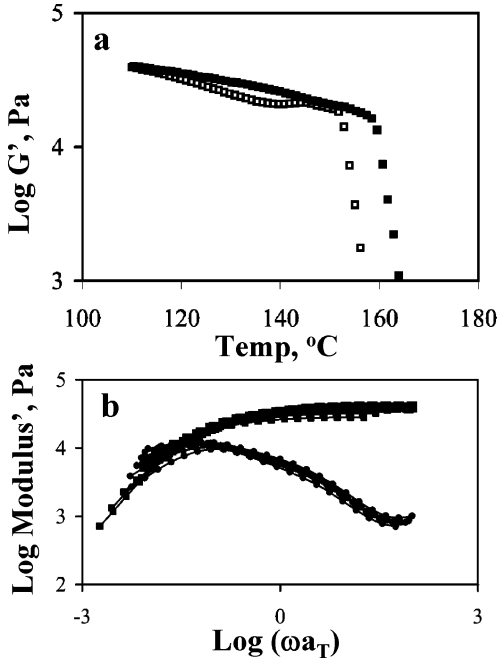

Figure 21. (a) Isochronal heating (■) and cooling (□) elastic modulus results for ISO-15b in the $Q^{214}-O^{70}$ overlapping region of Figure 1. The sharp drop in modulus at 166 °C (heating curve) is indicative of the ODT, and the inflection points on the heating and cooling curves are likely from structural rearrangements associated with the OOT. Here DMS is not sufficiently sensitive to characterize the OOT since the networks are mechanically similar. (b) TTS-shifted isothermal frequency spectra for ISO-15b in the $Q^{214}-O^{70}$ overlapping region in Figure 1 (T_{ref} = 130 °C). Data were acquired upon heating in 5 °C increments from 130 to 170 °C. G' (upper) and G'' (lower) curves are presented (data for disordered states are not shown). The large plateau modulus is consistent with a triply periodic structure.

Complementary DMS measurements, also conducted on ISO-15b, are shown in Figure 21. The upper panel displays isochronal (ω = 1 rad s^{-1}) G' data obtained while heating and cooling between 110 and 180 °C. A relatively featureless elastic plateau terminates in a precipitous drop in G' at 160 °C upon heating, with nearly complete recovery of the modulus by about 150 °C during cooling. This sequence of events, which we associate with the order−disorder transition, coincides with the hysteretic high-temperature optical transition found in Figure 20. The lower panel in Figure 21 shows time−temperature shifted isothermal frequency data measured at various temperatures below T_{ODT}. Comparisons with Figures 9, 13, and 18 suggest that the two lower temperature states identified in Figure 20 are triply periodic solids.

Combining the SAXS, birefringence, and DMS results leads us to conclude that the low- and high-temperature ordered phases in the overlap region of Figure 1 are Q^{214} and O^{70}, respectively; these materials disorder at the highest temperatures. The transition between these two network morphologies is remarkably facile, occurring at a rate comparable to other documented order−order transitions in the vicinity of the ODT, where epitaxial relationships have been implicated;[33,35,36] these include the G−Hex and Hex−BCC phase transitions.

IV. Level Set Modeling

The network phases characterized in this work, particularly O^{70}, feature complicated topologies that are

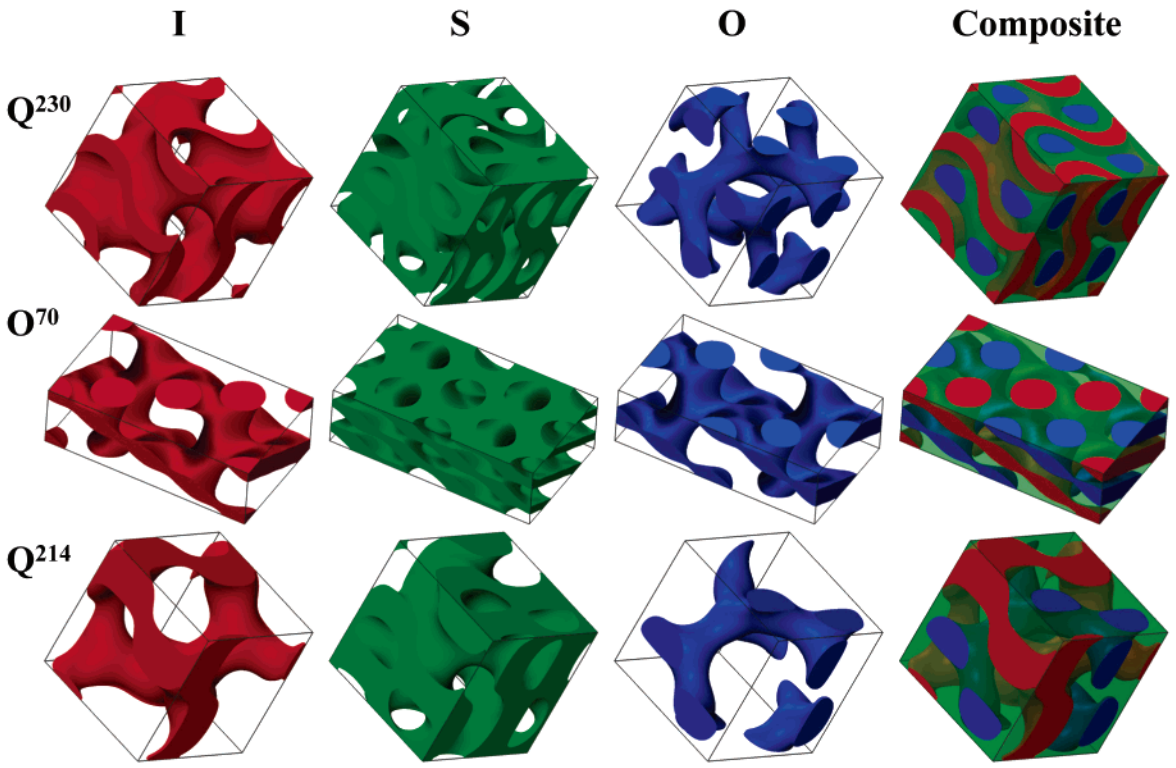

Figure 22. Space-filling models of the Q^{230}, O^{70}, and Q^{214} in ISO. The images in each row are constructed from isosurfaces of a triply periodic field generated by Fourier synthesis to have the correct space group symmetry. The first three columns correspond to the I, S, and O domains, respectively, while the fourth column shows the fully assembled structure. Volume fractions depicted here represent the experimental compositions of ISO-2a (Q^{230}), ISO-1c (O^{70}), and ISO-1a (Q^{214}).

difficult to visualize. X-ray scattering from a periodically ordered material generates a Fourier space representation of the electron density distribution, allowing measurement of the Bravais lattice and space group symmetry.[37] While this information can be unique to a given morphology, and often allows straightforward discernment between phases, visualization of the real-space structure is not possible using space group symmetry alone.

TEM contributes to the characterization process by producing two-dimensional projections of the full three-dimensional structure. This information, some of which is lost in projection, may be further convoluted by experimental factors: variations in sample thickness, orientation, staining, and instrument alignment can preclude the construction of a quantitative three-dimensional model.

We bridge the gap between the scattering-based reciprocal space representation and the microscopy-generated two-dimensional projections of real space using a Fourier synthesis technique, allowing the development and visualization of models of periodic structures.[37,38] This technique produces a numerical density field $S(\mathbf{x})$ with specified space group symmetry

$$S(\mathbf{x}) = \sum_{hkl} f_{hkl} E_{hkl}$$

$$E_{hkl} = \sum_{\alpha} e^{2\pi i \mathbf{T}_{\alpha}(\mathbf{x})\cdot\mathbf{G}_{hkl}} \qquad (1)$$

where f_{hkl} represents a complex structure factor that weights the contribution of each Fourier mode $\mathbf{G}_{hkl}$, with Miller indices h, k, and l. $\mathbf{T}(\mathbf{x})$ is the set of positions, in relative coordinates, equivalent to position $\mathbf{x}$ according to the space group symmetry (e.g., $Fddd$ has 16 equivalent, or general, positions). Single-crystal X-ray crystallography employs this construction to model electron densities at atomic resolution; each Bragg peak corresponds to a unique Fourier mode, the intensity of which is quantitatively related to the structure factor via $I \propto |f_{hkl}|^2$. In contrast, SAXS from block copolymers, under the best of circumstances, yields neither the quantity nor quality of individually identifiable Bragg reflections required to recover the precise electron density. Rather, we use arbitrarily chosen structure factors to generate fields $S(\mathbf{x})$ with the space group symmetry we derive from SAXS measurements. Constraining $S(\mathbf{x})$ to a value s_{ij} defines an isosurface (or level set), which may serve as a model intermaterial-dividing surface (IMDS) for domains i and j.

We have modeled the various ISO morphologies using this technique, choosing s_{IS} and s_{SO} such that the resultant surfaces entrap the experimentally measured volume fractions. Figure 22 shows space-filling models for the Q^{230} (first row), O^{70} (second row), and Q^{214} (third row) morphologies with compositions according to ISO-2b, ISO-9a, and ISO-15a, respectively. The images in each row were generated from a single construction of $S(\mathbf{x})$ with the appropriate space group symmetries: $Ia\bar{3}d$, $Fddd$, and $I4_132$. The I domain is defined in the first column for $S(\mathbf{x}) < s_{IS}$. The second and third columns depict the S ($s_{IS} < S(\mathbf{x}) < s_{SO}$) and O ($s_{SO} < S(\mathbf{x})$) domains, respectively. The fourth column assembles the separate domains into a single structure representing the composite block copolymer morphology. Details of the field construction and the domain shading scheme used in Figure 22 appear in Table 2.

We are able to directly compare these real-space models to the TEM data that appear in section III. TEM of the structures in Figure 22 may be simulated by

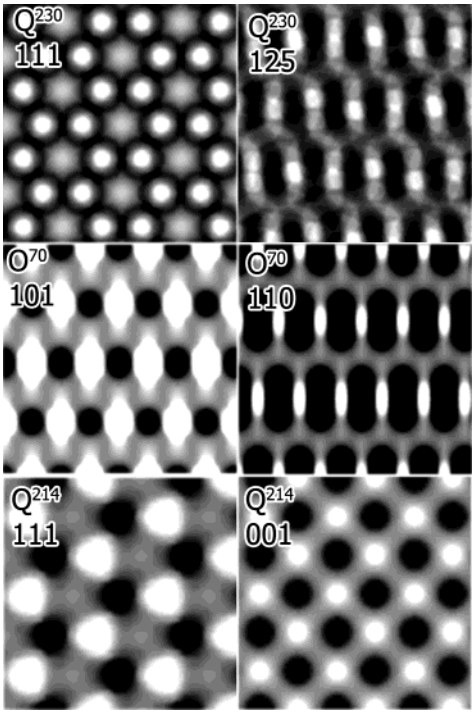

Figure 23. Simulated TEM projections at compositions corresponding to the experimental micrographs in Figures 7, 11, and 16 (ISO-2a, ISO-1c, and ISO-1a, respectively). Projections were integrated through the same fields from which the isosurface models in Figure 22 were generated. Simulations (representing ~75 nm slices) are labeled according to morphology and direction.

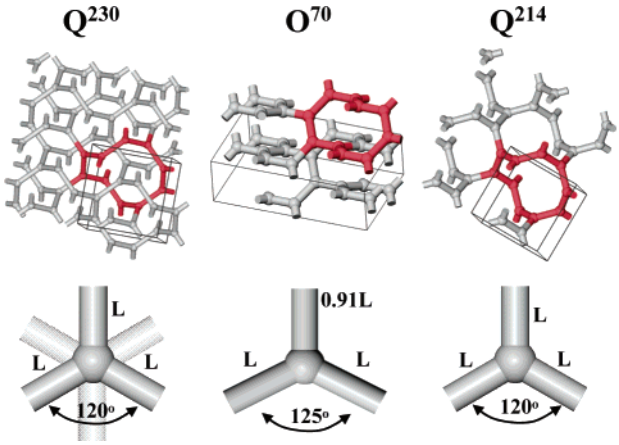

Figure 24. Upper row: ball-and-stick models for the Q^{230}, O^{70}, and Q^{214} networks. These models define the lattices populated by ISO polymer chains which form the morphology. A single (10,3) net is highlighted in each panel. Lower row: the corresponding trivalent connector from which each net is constructed. For Q^{214} and Q^{230}, the struts have 3-fold symmetry with a 120° bond angle and length $L = d_{001}\sqrt{2}/4$. The O^{70} connector has a mirror plane, with the largest bond angle equal to 125° and the long strut length $L = 0.18c$ when Wyckoff coordinate $z = {}^1/_{24}$. The shorter strut length is $0.91L$.

assigning dark (I domains) and bright (S and O domains) contrast levels, in accordance with the experimental contrast of OsO_4-stained ISO. Integrating the contrast level through a sample volume of constant thickness simulates the two-dimensional projection of TEM experiments. Figure 23 shows two projections for each network morphology; the scale and direction of projection shown in each panel were chosen to coincide with the TEM micrographs in the Results section (Figures 7, 11, and 16). Directional assignments of the experimental micrographs are based on these simulation results.

The excellent degree of congruity between simulated and experimental TEM data provides additional support to our morphological assignments. The [111] simulation of Q^{230} correctly reproduces the "wagon wheel" pattern, which belongs to the p6 plane group and appears as bright spots situated on the vertexes of tiled hexagons (compare to Figure 7a). The [125]-Q^{230} projection is unique in that the appearance and apparent symmetry of this image depend on the sample thickness; the simulation thickness used in Figure 23 corresponds to ca. 75 nm (about 1.5 unit cells), roughly the sample thickness used in TEM experiments (Figure 7b).

The [125]-Q^{230} simulation and micrograph bear a striking similarity to the [110]-O^{70} projection, the simulation of which appears in Figure 23 (second row, second column). Simulation reveals that these projections are clearly different, although drawing the same conclusion by comparison of the corresponding experimental micrographs (Figures 7b and 11a) requires careful inspection and ideally a complete three-dimensional topographical analysis.[40,41] [110]-O^{70} contains pmg plane group symmetry and represents the most common projection observed in TEM. The [101]-O^{70} simulation (first column, second row, Figure 23) also has pmg plane group symmetry, in agreement with the TEM micrograph in Figure 11b. This projection also is potentially misleading since overexposure of the image masks the interconnectivity between bright spots, making the image appear as if it belonged to the p3m1 plane group, corresponding to the [111]-Q^{214} projection. The favorable comparison between the O^{70} TEM simulation results and experimental micrographs provides further corroboration of relative lattice dimensions measured from SAXS experiments as well as the topology of the network structure.

Q^{214} TEM simulations appear in the lower row of Figure 23. The [111]-Q^{214} projection has p3m1 symmetry, clearly distinguishable from [111]-Q^{230}, and is congruent with Figure 16b. [001]-Q^{214} has p4m sym-

Table 2. Lattice Parameters, Field Construction, and Domain Assignment Scheme Used in the Level Set Models of Figure 22 and the TEM Simulations of Figure 23

space group	lattice constants	density field	isovalue	domain assignment	f_i
$Ia\bar{3}d$ (Q^{230})	$a = b = c$; $\alpha = \beta = \gamma = 90°$	$S(\mathbf{x}) = E_{112} + 0.25E_{022}$	$s_{IS} = 1.9$	$\rho_I(\mathbf{x}) = 1$: $S(\mathbf{x}) < s_{A/B}$	0.46
				$\rho_S(\mathbf{x}) = 1$: $s_{I/S} < S(\mathbf{x}) < s_{S/O}$	0.34
			$s_{SO} = 19.7$	$\rho_O(\mathbf{x}) = 1$: $S(\mathbf{x}) > s_{S/O}$	0.20
$Fddd$ (O^{70})	$a = 0.30c$; $b = 0.58c$; $\alpha = \beta = \gamma = 90°$	$S(\mathbf{x}) = E_{111} + 0.2E_{022} + 0.10E_{004} - 0.2E_{202} - 0.3E_{220} + 0.3E_{222}$	$s_{IS} = 16.9$	$\rho_I(\mathbf{x}) = 1$: $S(\mathbf{x}) > s_{A/B}$	0.45
			$s_{SO} = -1.1$	$\rho_S(\mathbf{x}) = 1$: $s_{I/S} > S(\mathbf{x}) > s_{S/O}$	0.40
				$\rho_O(\mathbf{x}) = 1$: $S(\mathbf{x}) < s_{S/O}$	0.15
$I4_132$ (Q^{214})	$a = b = c$; $\alpha = \beta = \gamma = 90°$	$S(\mathbf{x}) = (1 + i)E_{011} + 0.30(1 + i)E_{121}$	$s_{IS} = -17$	$\rho_I(\mathbf{x}) = 1$: $S(\mathbf{x}) < s_{A/B}$	0.17
				$\rho_S(\mathbf{x}) = 1$: $s_{I/S} < S(\mathbf{x}) < s_{S/O}$	0.50
			$s_{SO} = 9.7$	$\rho_O(\mathbf{x}) = 1$: $S(\mathbf{x}) > s_{S/O}$	0.33

metry in accordance with Figure 16a.

Inspection of the topologies represented by these structures reveals that each is a (10,3) uniform connected net. In general, an (*n*,*p*) net is assembled by tiling loops constructed from *n* planar connectors of valency *p* (Wells' notation).[39] The top row in Figure 24 shows a ball-and-stick representation for each topology, with a single (10,3) loop identified for clarity. Q^{214} is an example of the chiral (10,3)a network, and Q^{230} is simply two enantiomeric (10,3)a nets related by inversion symmetry.[39] The O^{70} network is an altogether different topology belonging to the (10,3)c class.[39]

Calculation of the geometry of the trivalent connector in these networks may be estimated using the fact that the nodes of the (10,3)c connectors (the "balls" in Figure 24, upper row) lie on Wyckoff position 16g, ($^1/_8$, $^1/_8$, *z*). For this position, $z \in [0,{}^1/_8)$; $z = {}^1/_8$ corresponds to position 8a, and values $z > {}^1/_8$ are redundant representations. The influence of this parameter is best understood by considering the (110)-O^{70} TEM projection, Figure 11a, and the corresponding simulation in Figure 23. The gray "zigzag" pattern between the bright elliptical spots appears to be constructed of roughly 3-fold connectors. The apexes of this pattern define the *z* value. The bright ovals correspond to the *Fddd*-8a position with $z = {}^1/_8$, and the midpoint of the "zigzag" is $z = 0$. The trivalent junction that defines this pattern is planar with mirror-plane symmetry; the bond lengths and angles are determined by the selection of *z* (which is in turn determined by the construction of $S(\mathbf{x})$). Under the experimentally determined lattice constants, 3-fold connector symmetry is not possible. The value used here, $z = {}^1/_{24}$, is intermediate to values that lead to equal bond lengths and equal bond angles, which is physically reasonable and consistent with Figures 6 and 11a. With this *z* value the O^{70} connector contains a 125° bond angle with one connector 91% of the length of the others. In contrast, both the Q^{214} and Q^{230} nets feature a rigorously 3-fold connector as the basic structural element. The connector element for each network phase appears in the lower row of Figure 24.

The mathematically symmetric models presented in this section demonstrate a technique that is useful in unifying SAXS data with the real-space representation afforded by TEM. Three-dimensional visualizations of these models provide topological information, and the resulting 2D projections are indispensable in the analysis of TEM data. The similarities that we observe in micrographs from different ordered morphologies emphasize that TEM images, while useful depictions of the real-space structure, cannot be used exclusively to identify complicated architectures.

V. Discussion

Figure 1 summarizes the findings of this experimental investigation. Nested between two-domain (I and S/O) and three-domain (I, S, and O) lamellae is a channel of multicontinuous and triply periodic network phases. We believe this discovery provides both practical and conceptual insights into the principles governing the self-assembly of block copolymer melts, as discussed in this section.

Poly(isoprene), poly(styrene), and poly(ethylene oxide) were chosen for this investigation for several reasons. Foremost is a nearly symmetric distribution of segment−segment interaction parameters, $\chi_{SO} \approx \chi_{IS} < \chi_{IO}$, which favors the formation of two interfaces (I−S and S−O) when these polymers are configured in the ISO architecture. (Also important, and discussed elsewhere,[5] is the opportunity to change to the SIO sequence, which introduces different rules for self-assembly leading to morphologies with three interfaces.) The magnitude of the χ parameters places the order−disorder transition at experimentally tractable temperatures when the overall molecular weight of these compounds is between roughly 15 000 and 25 000 g/mol, a convenient range for experimental characterization, yet high enough to permit comparison with mean-field theory. Additional advantages associated with this system include preferential staining by OsO_4; an S-block glass transition temperature that exceeds the O-block crystallization temperature, which minimizes microstructure distortion at room temperature; and relatively fast chain dynamics that facilitates phase equilibration. Also, the two-step synthesis procedure permits preparation of nearly monodisperse homologous sets of polymers along isopleths, which amplifies access to model compounds and provides additional control over composition variations between samples. These factors each have contributed to the comprehensive message encapsulated in Figure 1.

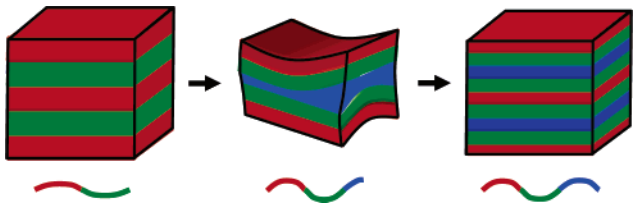

Figure 25. An illustration of our strategy for inducing network formation in ABC triblock copolymers. Each panel depicts a small area of the block copolymer interfacial structure. The left and right panels depict the flat interfaces that are preferred for symmetric compositions. Intermediate amounts of the C block (green) destabilize the flat B/C interface, leading to a saddle surface element.

This study was motivated by a desire to establish the molecular design principles for network formation in block copolymer melts. We speculated that adding a third block to a symmetric diblock copolymer, with a symmetric sequence of χ parameters (this situation has been referred to as nonfrustrated[42]), would create a situation that favors interfaces with hyperbolic curvature (i.e., saddle surfaces). Figure 25 illustrates this concept. Compositionally symmetric AB diblock ($f_A = f_B$) and ABC triblock ($f_A = f_B = f_C$) copolymers form two-domain (A = red and B = green) and three-domain (red, green, and C = blue) lamellae, respectively. Addition of asymmetric amounts of the C block to symmetric AB diblock creates competing packing constraints. While the equal sized A and B blocks prefer a flat interface, a smaller C block should favor a B−C interface with a finite spontaneous curvature. There are many ways to satisfy both conditions simultaneously under the constraint of constant density, although current theory does not offer predictive guidance. For example, alternating layers of cylinders and lamellae seems like an intuitively feasible solution. Apparently, negative interfacial Gauss curvature best accommodates these coupled conditions, which drives three-dimensional network formation.

The three network phases reported here are topologically similar. In each case the smallest structural building block is a trivalent connector. The cubic lattices (Q^{230} and Q^{214}) are constructed from symmetric nodes, while SAXS analysis indicates a slightly asymmetric connector with mirror-plane symmetry for the O^{70}

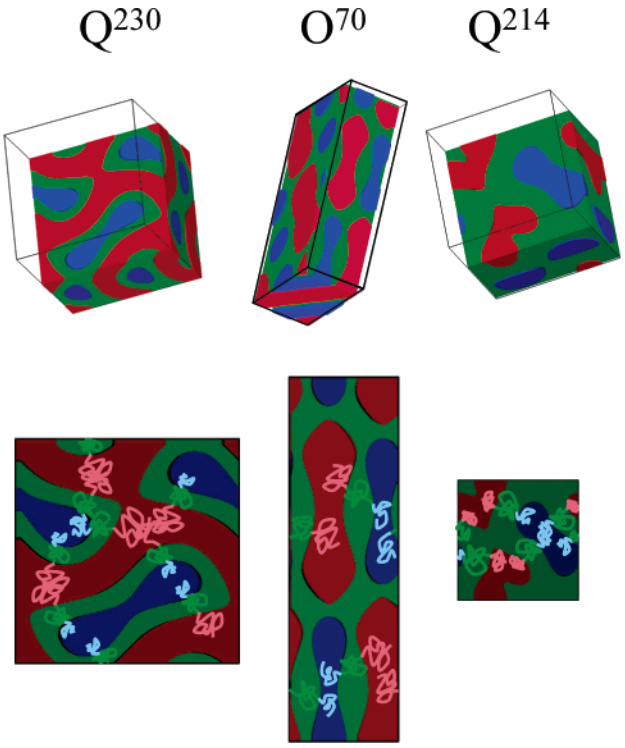

Figure 26. Top row: single unit-cell models of Q^{230}, O^{70}, and Q^{214} cross-sectioned to reveal the interfacial configuration. Bottom row: direct projections of the cross-sectioned interfaces. Sketches of ISO chains show how each morphology is assembled. Projections appear to scale; that is, the Q^{230} unit cell is roughly twice the thickness of O^{70} and Q^{214}.

structure (see Figure 23). At the next level of organization 10 trivalent connectors are assembled into (10,3) nets, which tile space in a regular manner consistent with the associated space group operations, resulting in one double (Q^{230}) and two single (O^{70} and Q^{214}) network lattices. To complete the morphologies, ISO triblock copolymer is added to these lattices subject to an incompressibility constraint. We have modeled these space-filling configurations using level set calculations (see section IV) based on the space group assignments derived from SAXS data and the experimental block volume fractions. This approach does not account for the underlying molecular factors that govern the thermodynamics of microphase separation, i.e., contributions to the overall free energy due to interfacial area (enthalpy) and chain stretching (entropy). Accurate composition profiles require a proper statistical mechanical analysis, such as self-consistent mean-field theory.[43] Nevertheless, level set models provide useful insights into the spatial arrangement of domains and can capture the qualitative morphological features associated with specific packing symmetries as illustrated in Figure 22.

We further explore the nature of the network channels by comparing two-dimensional cuts through the level set models. Figure 26 illustrates three such examples, where the upper row presents space-filling level set models, cross-sectioned to reveal the nature of the interfaces. The lower row contains a direct projection of each exposed cross section; sketches of individual ISO chains elucidate the manner in which they populate the morphology. These cross sections appear to scale; that is, the Q^{230} lattice constant is roughly double that of both the Q^{214} lattice and the *a* axis of O^{70}. Inspection of these two-dimensional patterns reveals an obvious deficiency in the level set constructions: relatively wide variations in domain dimensions. For example, all three domains spaces in the O^{70} projection display at least 2-fold variations in dimensions; this is particularly acute with the middle (green) block. Self-consistent mean-field theory has demonstrated that uniform domain dimensions are a unifying feature of block copolymer self-assembly,[44] arising from the optimization of interfacial energy and chain stretching in monodisperse melts.

The pentacontinuous Q^{230} phase, a three-color analogue to the two-color double gyroid in diblock copolymers, occurs in ISO polymers with compositions that strictly obey $f_I > f_S > f_O$. Specimens with this compositional sequencing prefer a "core−shell" interfacial configuration: parallel I/S and S/O interfaces that enclose the O domain. The Q^{230} lattice consists of two enantiomeric (10,3)a nets, each of which represents an O-rich region surrounded by the S domain, with I as the matrix component (see Figure 22, first row, and Figure 26, first column). The two networks that compose this centrosymmetric morphology lead to the formation of two distinct O and S domains.

On the styrene-rich portion of the network channel lies the Q^{214} phase, also known as the alternating gyroid morphology. Self-consistent-field theory calculations by Matsen indicate stability of this phase in ABC triblocks when $f_A = f_C$ and $\chi_{AB} = \chi_{BC} < \chi_{AC}$;[20] the occurrence of Q^{214} in the ISO system is roughly consistent with these conditions. Matsushita et al. have confirmed these calculations in various experiments on ISV polymers located along the $f_A = f_C$ isopleth (dashed line in Figure 1).[9,11,19] In the present work, this phase persists well into the O-lean side of the $f_I = f_O$ isopleth, which may indicate either a large region of Q^{214} stability in general or that conformational asymmetry (i.e., disparities among block statistical segment lengths) has shifted the phase boundary.[45−47] In Q^{214}-forming ISO, the S domain (middle block) accounts for the greatest volume fraction; accordingly, the I/S and S/O interfaces are (on average) oppositely curved. Referring to Figure 22, Q^{214} is topologically equivalent to Q^{230} in that both lattices feature two enantiomeric (10,3)a nets. However, in Q^{214} each net is chemically distinct; i.e., the I block populates one net while the O block occupies the other (see Figure 26, right column), leading to a chiral, noncentrosymmetric structure. Because the enantiomeric (10,3)a nets in Q^{214} are spanned by a single ABC block copolymer chain, it becomes intuitive that the Q^{214} lattice dimension is roughly half that of Q^{230}, whose (10,3)a nets are bridged by two polymer chains.

Q^{214} and Q^{230} are unstable in the central portion of the ISO phase portrait. Here, the I and S domains become comparable in size, and the degree of curvature required to assemble the I block into a (10,3)a topology presumably incurs a destabilizing elastic penalty. Our experiments show that the O^{70} morphology best accommodates these intermediate compositions, allowing the optimization of elastic energy and interfacial tension by providing varying degrees of interfacial curvature. The formation of O^{70} in samples with accessible order−order or order−disorder transitions is always reversible, a compelling argument in support of this phase as an equilibrium structure. The birefringence data for ISO-15b (Figure 19) perhaps best illustrates this reversibility. These data show the facile conversion from Q^{214} to O^{70} to disorder with increasing temperature, followed by the reverse sequence with decreasing temperature.

The substantial range of compositions over which O^{70} forms, in addition to its discovery in poly(cyclohexylethylene-*b*-ethylethylene-*b*-ethylene),[23] supports the notion that O^{70} is a universal morphology in ABC triblock copolymers. Our data suggest that the widespread stability of O^{70} may be attributable in part to the permissibility of relative lattice dimension variations, with respect to composition and temperature. Orthorhombic structures retain their symmetry upon extensional or compressive transformations, giving O^{70} two additional degrees of freedom compared to cubic morphologies. Up to 2.5% variation in the lattice parameters *a*/*c* and *b*/*c* is identified in Table 1.

Level set models of O^{70} (Figure 22, middle row) offer additional insights into the geometry of this fascinating morphology. As with any crystal structure, O^{70} is formed by combining a basis with a lattice. Here the lattice is the *Fddd* network (see Figure 23), and the basis consists of segregated triblock copolymer, with the I (or O) ends positioned along the (10,3)c net. (This morphology can be envisioned as containing two interpenetrating (10,3)c nets, related by translation, which form the disproportionately sized I and O domains (see Figure 26, middle column), separated by a "matrix" of S.) The (10,3)c topology has a reduced curvature with respect to (10,3)a. Both networks are constructed from planar, trivalent connectors assembled into 10-node loops. The dihedral angle between all connectors in the (10,3)a topology (Q^{214} and Q^{230}) is 70.5°. However, for (10,3)c (O^{70}), 6 of the 10 connections in the (10,3) loop feature a dihedral angle of 0°, with a tilt of approximately 73.6° in the remaining four. (This value is a function of the *a* and *c* lattice dimensions: $\tan^{-1}(c/a)$.) Furthermore, the (10,3)a connector has strict 3-fold symmetry, whereas the (10,3)c connector contains only mirror planes (see Figure 23, bottom row).

The deviation from cubic symmetry in block copolymer network morphologies is a particularly striking aspect of O^{70}. Self-assembly in block copolymers is often compared to oil/water/surfactant mixtures. Both form network structures under the appropriate conditions, but in surfactant mixtures, all known network morphologies are cubic. The organizing force that dominates self-assembly in surfactants (minimization of interfacial area) is completely isotropic; thus, the resulting structures have no unique axis. In block copolymers, however, the elastic energy required to pack polymer chains onto a minimal surface can be quite large. Free of this constraint, surfactant mixtures may select between cubic networks constructed from trivalent (Q^{230}), tetravalent (Q^{224}, $Pn\bar{3}m$), and hexavalent (Q^{229}, $Im\bar{3}m$) connectors to minimize the interfacial contact between phases.[48−54] However, in neat linear block copolymers, only triply coordinated junctions have been found. We speculate that the higher-coordination connectors are unfavorable in neat linear block copolymers because forming such topologies would require excessive chain stretching. As a result, the number of possible cubic structures is limited, and the system adopts O^{70} as an alternative triply periodic structure to minimize the free energy.

On the basis of the demonstrated universal nature of diblock copolymer self-assembly,[46] we anticipate that the phase behavior illustrated in Figure 1 will be manifested in other linear ABC triblock copolymers. In fact, already we have found the O^{70} phase (along with another, probably metastable, orthorhombic phase referred to as O^{52}) in a saturated hydrocarbon system,[23] and reanalysis of SAXS and TEM data obtained from a poly(styrene-*b*-isoprene-*b*-dimethylsiloxane) (SID) triblock copolymer indicates another occurrence.[55] (The SID specimen has a composition of 0.20/0.59/0.21 and approximately the same relative sequence of χ parameters as ISO.) Notwithstanding these findings, we hasten to caution against assuming that the precise phase boundaries identified in Figure 1 will translate to other systems. This phase behavior is governed by two interfacial surfaces and may be sensitive to the ratio χ_{AB}/χ_{BC} as well as to variations in the block statistical segment lengths. Our experience with salt-doped ISO and SIO underscores this point.[56,57] Until the roles of these parameters have been evaluated by self-consistent mean-field theory, we cannot offer a precise prescription for creating specific network morphologies from arbitrary block types.

VI. Conclusions

Using a comprehensive collection of characterization and modeling techniques, we detail the equilibrium phase behavior of ISO in the large composition space spanning symmetric IS diblock and ISO triblock copolymers. Located between the two- and three-domain lamellar morphologies lies a wide channel of network morphologies composed of hyperbolic (saddle) interfacial surfaces. Three distinct phases, cubic Q^{230} (core−shell double gyroid), orthorhombic O^{70}, and cubic Q^{214} (alternating gyroid), are formed as the composition varies from I-rich to S-rich across the phase diagram. Level set models, along with experimental TEM micrographs, show that each network is comprised of ordered arrays of trivalent connected 10-node loops that form triply periodic lattices. An expansive O^{70} network region represents a significant departure from the behavior reported in surfactant systems, which we trace to the molecular packing conditions that govern microphase separation in block copolymer melts: optimization of interfacial area and elastic chain stretching. These results provide a framework for the development of a universal ABC phase diagram when $\chi_{AB} \approx \chi_{BC} < \chi_{AC}$.

Acknowledgment. This work was supported by the NSF through Grant DMR-0220460. Graduate fellowships to T.H.E. (Lucent Technologies), E.W.C. (NSF), and C.M.H. (NSF) are gratefully acknowledged. Use of the Advanced Photon Source at Argonne National Labs was supported by the U.S. Department of Energy, Basic Energy Sciences, Office of Science, under Contract W-31-109-Eng-38. This research program has made extensive use of the MRSEC (NSF) supported Institute of Technology Characterization Facility at the University of Minnesota, Twin Cities Campus.

Appendix. Structure Factor of Compositionally Symmetric Lamellae

In general, the relationship between the scattering intensity from a perfectly periodic electron density field $\rho(\mathbf{r})$ and the scattering wavevector $\mathbf{q}$ is

$$I \propto |F(\mathbf{q})\, S(\mathbf{q})|^2$$

$$F(\mathbf{q}) = \begin{cases} 1: & \mathbf{q} = 2\pi\mathbf{G}_{hkl} \\ 0: & \mathbf{q} \neq 2\pi\mathbf{G}_{hkl} \end{cases}$$

$$S(\mathbf{q}) = \int_V \mathrm{d}\mathbf{r}\, \rho(\mathbf{r})\, \mathrm{e}^{2\pi i \mathbf{G}_{hkl}\cdot\mathbf{r}} \qquad (2)$$

$F(\mathbf{q})$ is the form factor, which enforces the Laue condition that diffraction occurs only when $\mathbf{q}$ is a reciprocal lattice vector $\mathbf{G}_{hkl}$. The structure factor $S(\mathbf{q})$ is the Fourier transform of the electron density field within the unit cell volume V. For the one-dimensional centrosymmetric lamellae considered in this work, wavevectors G_{hkl} become

$$G_{hkl} = \frac{h}{d} \qquad (3)$$

where h is the Miller index and d is the length of a single unit cell. Considering only cases where $F(\mathbf{q}{=}2\pi h/d) = 1$, expression 2 becomes a simple one-dimensional integral:

$$I(h) \propto \left| \int_0^d \mathrm{d}r\, \rho(r)\, \mathrm{e}^{2\pi i (h/d) r} \right|^2 = \left| \int_0^1 \mathrm{d}x\, \rho(x)\, \mathrm{e}^{2\pi i h x} \right|^2 \qquad (4)$$

where $x = r/d$. Invoking inversion symmetry yields

$$I(h) \propto \left| \int_0^{1/2} \mathrm{d}x\, \rho(x)(\mathrm{e}^{2\pi i h x} + \mathrm{e}^{-2\pi i h x}) \right|^2 = \left| \int_0^{1/2} \mathrm{d}x\, \rho(x)(\cos(2\pi h x) + \cos(-2\pi h x)) \right|^2 \qquad (5)$$

Note that the imaginary sine terms always cancel for centrosymmetric structures.

For strongly segregated, perfectly symmetric two-domain lamellae the electron density field may be expressed as the step function

$$\rho(x) = \begin{cases} \rho_A: & x \in \left[0, \frac{1}{4}\right] \\ \rho_B: & x \in \left(\frac{1}{4}, \frac{1}{2}\right] \end{cases} \qquad (6)$$

For this definition of $\rho(x)$ eq 5 may be integrated to yield the analytic expression

$$I \propto \left| \frac{1}{h\pi} \left(\rho_A - \rho_B + 2\rho_B \cos(h\pi/2) \right) \sin(h\pi/2) \right|^2 \qquad (7)$$

which indicates an analytical extinction when $h = 2n$, where n is an integer. This is consistent with the near absence of $q/q^* = 2$ in the LAM_2 scattering data presented in Figure 2.

For strongly segregated, perfectly symmetric three-domain lamellae the electron density field may be expressed as the step function

$$\rho(x) = \begin{cases} \rho_A: & x \in \left[0, \frac{1}{6}\right] \\ \rho_B: & x \in \left(\frac{1}{6}, \frac{1}{3}\right] \\ \rho_C: & x \in \left(\frac{1}{3}, \frac{1}{2}\right] \end{cases} \qquad (8)$$

For this definition of $\rho(x)$ eq 5 may be integrated to yield the analytic expression

$$I(h) \propto \left| \frac{1}{h\pi} (\rho_A - \rho_B + \rho_C + 2(\rho_B - \rho_C) \cos(h\pi/3) + 2\rho_C \cos(2h\pi/3)) \sin(h\pi/3) \right|^2 \qquad (9)$$

which predicts structure factor extinctions for $q/q^* = 3n$, also in agreement with the data for the LAM_3 structure in Figure 2.

References and Notes

(1) Bates, F. S.; Fredrickson, G. H. *Phys. Today* **1999**, *52*, 32−38.
(2) Khandpur, A. K.; Foerster, S.; Bates, F. S.; Hamley, I. W.; Ryan, A. J.; Bras, W.; Almdal, K.; Mortensen, K. *Macromolecules* **1995**, *28*, 8796−8806.
(3) Davidock, D. A.; Hillmyer, M. A.; Lodge, T. P. *Macromolecules* **2003**, *36*, 4682−4685.
(4) Matsen, M. W.; Bates, F. S. *Macromolecules* **1996**, *29*, 1091−1098.
(5) Bailey, T. S.; Pham, H. D.; Bates, F. S. *Macromolecules* **2001**, *34*, 6994−7008.
(6) Breiner, U.; Krappe, U.; Abetz, V.; Stadler, R. *Macromol. Chem. Phys.* **1997**, *198*, 1051−1083.
(7) Hueckstaedt, H.; Goldacker, T.; Goepfert, A.; Abetz, V. *Macromolecules* **2000**, *33*, 3757−3761.
(8) Huckstadt, H.; Gopfert, A.; Abetz, V. *Polymer* **2000**, *41*, 9089−9094.
(9) Mogi, Y.; Nomura, M.; Kotsuji, H.; Ohnishi, K.; Matsushita, Y.; Noda, I. *Macromolecules* **1994**, *27*, 6755−6760.
(10) Seki, M.; Suzuki, J.; Matsushita, Y. *J. Appl. Crystallogr.* **2000**, *33*, 285−290.
(11) Suzuki, J.; Seki, M.; Matsushita, Y. *J. Chem. Phys.* **2000**, *112*, 4862−4868.
(12) Avgeropoulos, A.; Paraskeva, S.; Hadjichristidis, N.; Thomas, E. L. *Macromolecules* **2002**, *35*, 4030−4035.
(13) Mani, S.; Weiss, R. A.; Cantino, M. E.; Khairallah, L. H.; Hahn, S. F.; Williams, C. E. *Eur. Polym. J.* **1999**, *36*, 215−219.
(14) Ludwigs, S.; Boeker, A.; Voronov, A.; Rehse, N.; Magerle, R.; Krausch, G. *Nature Mater.* **2003**, *2*, 744−747.
(15) Breiner, U.; Krappe, U.; Thomas, E. L.; Stadler, R. *Macromolecules* **1998**, *31*, 135−141.
(16) Stadler, R. T.; Auschra, C.; Bechmann, J.; Krappe, U.; Voigt-Martin, I.; Leibler, L. *Macromolecules* **1995**, *28*, 3080−3097.
(17) Beckmann, J.; Auschra, C.; Stadler, R. *Macromol. Rapid Commun.* **1994**, *15*, 67−72.
(18) Shefelbine, T. A.; Vigild, M. E.; Matsen, M. W.; Hajduk, D. A.; Hillmyer, M. A.; Cussler, E. L.; Bates, F. S. *J. Am. Chem. Soc.* **1999**, *121*, 8457−8465.
(19) Mogi, Y.; Mori, K.; Matsushita, Y.; Noda, I. *Macromolecules* **1992**, *25*, 5412−5415.
(20) Matsen, M. W. *J. Chem. Phys.* **1998**, *108*, 785−796.
(21) Bailey, T. S.; Hardy, C. M.; Epps, T. H., III.; Bates, F. S. *Macromolecules* **2002**, *35*, 7007−7017.
(22) Epps, T. H., III.; Cochran, E. W.; Hardy, C. M.; Bailey, T. S.; Waletzko, R. S.; Bates, F. S. *Macromolecules* **2004**, *37*, 7085−7088.
(23) Cochran, E. W.; Bates, F. S. *Phys. Rev. Lett.* **2004**, *93*, 087802.
(24) Hillmyer, M. A.; Bates, F. S. *Macromolecules* **1996**, *29*, 6994−7002.
(25) Fetters, L. J.; Lohse, D. J.; Richter, D.; Witten, T. A.; Zirkel, A. *Macromolecules* **1994**, *27*, 4639−4646.
(26) Balsara, N. P.; Garetz, B. A.; Dai, H. J. *Macromolecules* **1992**, *25*, 6072−6074.
(27) Balsara, N. P.; Perahia, D.; Safinya, C. R.; Tirrell, M.; Lodge, T. P. *Macromolecules* **1992**, *25*, 3896−3901.
(28) Wieczorek, W.; Raducha, D.; Zalewska, A.; Stevens, J. R. *J. Phys. Chem. B* **1998**, *102*, 8725−8731.
(29) Goldacker, T.; Abetz, V. *Macromol. Rapid Commun.* **1999**, *21*, 16.
(30) Hajduk, D. A.; Harper, P. E.; Gruner, S. M.; Honecker, C. C.; Kim, G.; Thomas, E. L.; Fetters, L. J. *Macromolecules* **1994**, *27*, 4063−4075.
(31) Hamley, I. W.; Fairclough, J. P. A.; Ryan, A. J.; Mai, S. M.; Booth, C. *Phys. Chem. Chem. Phys.* **1999**, *1*, 2097−2101.

(32) Vigild, M. E.; Almdal, K.; Mortensen, K.; Hamley, I. W.; Fairclough, J. P. A.; Ryan, A. J. *Macromolecules* **1998**, *31*, 5702−5716.
(33) Hajduk, D. A.; Ho, R.-M.; Hillmyer, M. A.; Bates, F. S.; Almdal, K. *J. Phys. Chem. B* **1998**, *102*, 1356−1363.
(34) Kossuth, M. B.; Morse, D. C.; Bates, F. S. *J. Rheol.* **1999**, *43*, 167−196.
(35) Koppi, K. A.; Tirrell, M.; Bates, F. S.; Almdal, K.; Mortensen, K. *J. Rheol.* **1994**, *38*, 999−1027.
(36) Schulz, M. F.; Bates, F. S.; Almdal, K.; Mortensen, K. *Phys. Rev. Lett.* **1994**, *73*, 86−89.
(37) Hahn, T., Ed. *International Tables for Crystallography*, 4th revised ed.; 1994; Vol. A.
(38) Wohlgemuth, M.; Yufa, N.; Hoffman, J.; Thomas, E. L. *Macromolecules* **2001**, *34*, 6083−6089.
(39) Wells, A. F. *Three-Dimensional Nets and Polyhedra*; John Wiley & Sons: New York, 1977.
(40) Spontak, R. J.; Fung, J. C.; Braunfeld, M. B.; Sedat, J. W.; Agard, D. A.; Ashraf, A.; Smith, S. D. *Macromolecules* **1996**, *29*, 2850−2856.
(41) Fung, J. C.; Kane, L.; Smith, S. D.; Sedat, J. W.; Agard, D. A.; Spontak, R. J. *Mater. Sci. Forum* **1997**, *239*−*241*, 179−184.
(42) Bailey, T. S. Doctoral Thesis, Department of Chemical Engineering and Materials Science, University of Minnesota, Minneapolis, MN, 2002.
(43) Matsen, M. W.; Schick, M. *Phys. Rev. Lett.* **1994**, *72*, 2660−2663.
(44) Matsen, M. W.; Bates, F. S. *Macromolecules* **1996**, *29*, 7641−7644.
(45) Matsen, M. W.; Schick, M. *Macromolecules* **1994**, *27*, 4014−4015.
(46) Bates, F. S.; Schulz, M. F.; Khandpur, A. K.; Foerster, S.; Rosedale, J. H. *Faraday Discuss.* **1995**, *98*, 7−18.
(47) Matsen, M. W.; Bates, F. S. *J. Polym. Sci., Part B: Polym. Phys.* **1997**, *35*, 945−952.
(48) Luzzati, V.; Mustacchi, H.; Skoulios, A.; Husson, F. *Acta Crystallogr.* **1960**, *13*, 660−667.
(49) Luzzati, V. *Biol. Membr.* **1968**, 71−123.
(50) Luzzati, V.; Tardieu, A.; Gulik-Krzywicki, T. *Nature (London)***1968**, *217*, 1028−1030.
(51) Winter, R.; Erbes, J.; Templer, R. H.; Seddon, J. M.; Syrykh, A.; Warrender, N. A.; Rapp, G. *Phys. Chem. Chem. Phys.* **1999**, *1*, 887−893.
(52) Seddon, J. M. *Biochemistry* **1990**, *29*, 7997−8002.
(53) Seddon, J. M.; Hogan, J. L.; Warrender, N. A.; Pebay-Peyroula, E. *Prog. Colloid Polym. Sci.* **1990**, *81*, 189−197.
(54) Landh, T. *FEBS Lett.* **1995**, *369*, 13−17.
(55) Sugiyama, M.; Shefelbine, T. A.; Vigild, M. E.; Bates, F. S. *J. Phys. Chem. B* **2001**, *105*, 12448−12460.
(56) Epps, T. H., III.; Bailey, T. S.; Pham, H. D.; Bates, F. S. *Chem. Mater.* **2002**, *14*, 1706−1714.
(57) Epps, T. H., III.; Bailey, T. S.; Waletzko, R.; Bates, F. S. *Macromolecules* **2003**, *36*, 2873−2881.

MA048762S